SCALE Modeling of the Sodium-Cooled Fast-Spectrum Advanced Burner Test Reactor

Alex Shaw
Friederike Bostelmann
Donny Hartanto
Erik Walker
William A. Wieselquist

**Approved for public release.
Distribution is unlimited.**

July 2023

OAK RIDGE
National Laboratory

Nuclear Energy and Fuel Cycle Division

SCALE MODELING OF THE SODIUM-COOLED FAST-SPECTRUM ADVANCED BURNER TEST REACTOR

Alex Shaw
Friederike Bostelmann
Donny Hartanto
Erik Walker
William A. Wieselquist

Date Published: July 2023

CONTENTS

LIST OF FIGURES

LIST OF TABLES

ABBREVIATIONS

β_{eff}	effective delayed neutron fraction
k_{eff}	effective neutron multiplication factor
ABTR	Advanced Burner Test Reactor
ANL	Argonne National Laboratory
BOEC	beginning of equilibrium cycle
CE	continuous energy
CSAS	Criticality Safety Analysis Sequence
EALF	energy of average lethargy of fission
EBR-I	Experimental Breeder Reactor I
EBR-II	Experimental Breeder Reactor II
EOEC	end of equilibrium cycle
FFTF	Fast Flux Test Facility
FHR	fluoride salt-cooled high-temperature reactor
HPR	heat pipe reactor
HTGR	high-temperature gas-cooled reactor
INL	Idaho National Laboratory
LFP	lumped fission product
LWR	light water reactor
MG	multigroup
MSR	molten salt reactor
MTIHM	metric ton initial heavy metal
NRC	Nuclear Regulatory Commission
ORNL	Oak Ridge National Laboratory
pcm	percent mille
PFNS	prompt fission neutron spectrum
PWR	pressurized water reactor
SFR	sodium-cooled fast reactor
SNL	Sandia National Laboratories
TRU	transuranics

ACKNOWLEDGMENTS

ABSTRACT

This report documents the modeling and simulation of a sodium-cooled fast reactor (SFR) as part of a U.S. Nuclear Regulatory Commission–sponsored project to assess the modeling and simulation capabilities for accident progression, source term, and consequence analysis for advanced reactor technologies with the Oak Ridge National Laboratory code SCALE and the Sandia National Laboratories (SNL) code MELCOR.

Based on publicly available benchmark specifications, a fully heterogeneous 3D SCALE model of the 250 MWth Advanced Burner Test Reactor (ABTR) was developed to demonstrate SCALE's capabilities for full-core reactivity analysis, fuel inventory prediction, and decay heat analysis of an SFR. The benchmark specifications contain modeling details for the ABTR core at the beginning of equilibrium cycle (BOEC) at operating conditions; they were derived from a 2006 preconceptual design report produced by Argonne National Laboratory. The ABTR was designed to demonstrate reactor-based transmutation of transuranics, that is, to "burn" transuranics recovered from light-water reactor (LWR) spent fuel. The ABTR's fuel is designed to operate in 4 month cycles using uranium/transuranic (U/TRU) metallic fuel, with a TRU content of approximately 20%, at a conversion ratio of approximately 0.6.

Various reactivity calculations were performed with SCALE for the ABTR and, where possible, compared with results available in the open literature. Additionally, SCALE was used to perform a full-core depletion calculation over the 4 month cycle to obtain the nuclide inventory at the end of equilibrium cycle (EOEC). These nuclide inventories, decay heat, power profiles, and reactivity feedback coefficients at EOEC represent the initial conditions for analyzing severe accident scenarios with MELCOR.

1. INTRODUCTION

The sodium-cooled fast reactor (SFR) is an advanced reactor with a key capability, compared to the light water reactor (LWR), to breed nuclear fuel by converting abundant fertile nuclides like ^{238}U to fissile nuclides like ^{239}Pu. The SFR can also be used to transmute long-living actinides in spent LWR fuel, most efficient in a fast neutron spectrum, which is achieved by a high fuel density and a high fuel volume fraction. To achieve a compact reactor core with a high power density, efficient heat removal is required which is achieved through a liquid sodium coolant, which has high heat capacity and conductivity and can operate at atmospheric pressure [15].

The first breeder reactor was the Experimental Breeder Reactor I (EBR-I), an SFR built to demonstrate the principle of breeding or producing more fissile material than is consumed. This 1.4 MWth reactor began operation in 1951 and was one of the first electricity-generating reactors worldwide. EBR-I was fueled by uranium metal plates, with a liquid sodium-potassium coolant. EBR-I suffered a partial meltdown, was repaired, and then shutdown a decade later. The reactor that followed was named the Experimental Breeder Reactor II (EBR-II), built to demonstrate that breeding fuel was feasible in a full-scale power reactor with a significantly higher power, 62.5 MWth. The reactor used uranium metal fuel rods and demonstrated multiple passive safety capabilities during transient events, with negative reactivity responses to increasing temperature. Additional historical SFR operations contributed to design aspects of current SFRs. For example, the Fast Flux Test Facility (FFTF), a 400 MWth mixed-oxide–fueled reactor, inspired the control assembly system, with a mechanically limited withdrawal rate to ensure controlled rod movement. Fermi 1, a 200 MWth prototype breeder reactor fueled with uranium metal, suffered a coolant flow blockage when a plate in the lower core became loose, restricting flow access and causing partial fuel melts. [30]

SFR modeling has historically been performed with deterministic, multigroup (MG) neutronics tools such as those developed by Argonne National Laboratory (ANL) [18]. In this work, we exercise the capability of the SCALE code system [29] to model SFR systems. SCALE is extensively validated for criticality, reactor physics, and radiation shielding applications. Although validation has been focused on water-moderated thermal spectrum systems, criticality validation also includes systems of intermediate and fast spectral conditions [28]. Previous SFR development and analysis efforts with SCALE included the analysis of the EBR-II [3] and the 1,000 MWth Advanced Burner Reactor benchmark [2], as well as the generation of MG nuclear data libraries specifically for SFRs [4] and fast reactors in general [10].

To assess the modeling and simulation capabilities for accident progression, source term, and consequence analysis for non–LWR technologies, the Nuclear Regulatory Commission (NRC) initiated a collaborative project between the U.S. NRC, Sandia National Laboratories (SNL), and Oak Ridge National Laboratory (ORNL) [21]. The SNL team continued to develop and use the computer code MELCOR [8] to perform severe accident progression and source term analyses for non-LWRs. The ORNL team used SCALE to provide MELCOR the detailed nuclide inventory, and to demonstrate SCALE's capabilities for inventory, decay heat, reactivity, power, and flux analysis of the various non-LWRs. The work presented in this report focuses on the application of SCALE for SFR analysis. This work follows previous studies in which SCALE was used for the simulation of heat pipe reactors (HPRs) [26], high-temperature gas-cooled reactors (HTGRs) [17], fluoride salt-cooled high-temperature reactors (FHRs) [1], and molten salt reactors (MSRs) [12]. The corresponding MELCOR studies are found in separate reports [24, 23, 25].

SFR analysis is demonstrated using the 250 MWth ABTR for which benchmark specifications are publicly available [11]. Additional information for this reactor design can be drawn from the detailed design report [6]. The ABTR was designed by ANL based on ANL's experience with designing, constructing, and operating SFRs as well as vast knowledge of SFR physics and simulation tool development. The ABTR was

designed to demonstrate reactor-based transmutation of transuranics (TRU), that is, to "burn" TRU recovered from spent LWR fuel. The ABTR's fuel is designed to operate in 4 month cycles using U/TRU-Zr10% metallic fuel, with a TRU content of approximately 20%, at a conversion ratio of approximately 0.6. The benchmark provides beginning of equilibrium cycle (BOEC) fuel compositions at operating conditions, with thermal expansion considered in the dimensions and material compositions. Great effort was taken to correctly model the system as described, though minor assumptions are noted. Verification of the SCALE model was performed through a comparison with results from a recent Idaho National Laboratory (INL) report [13]. Based on the verified model, SCALE was applied to determine reactivity, neutron flux, and power distributions of the full ABTR core. Fuel inventory after a 4 month long cycle—that is, at end of equilibrium cycle (EOEC)—was obtained based on a full-core depletion calculation. SCALE results of reactivity coefficients, power distributions, and nuclide inventories were provided to MELCOR to support analyses of potential severe accident scenarios. Based on the Fermi 1 experience, a coolant flow blockage scenario was considered both with SCALE and with MELCOR [16].

Section 2 provides an overview of the ABTR benchmark and a discussion of the minor assumptions made in developing the SCALE model. Section 3 provides verification of SCALE's effective neutron multiplication factor (k_{eff}) and β_{eff} results using results published in the open literature. Section 4 provides detailed SCALE analyses of the neutron flux and reactivity feedback of the BOEC ABTR core. Section 5 details the depletion of the full ABTR core to EOEC and the analysis of the nuclide inventory, decay heat, and power profiles at EOEC. Section 6 details the approach taken for the generation of ORIGEN libraries for the ABTR, which allows the rapid generation of fuel inventory for this reactor with SCALE's ORIGAMI code.

The models and scripts developed for this work are available on the public Gitlab repository associated with the overarching NRC project: https://code.ornl.gov/scale/analysis/non-lwr-models-vol3.

2. ADVANCED BURNER TEST REACTOR

The following sections provide a brief overview of the modeling basis for the ABTR benchmark. Details can be found in the benchmark specification [11] and the design report [6].

2.1 BENCHMARK MODEL

The core description used in this analysis is derived from the ABTR benchmark specification [11] and the associated design report [6]. The ABTR benchmark details the core configuration, ignoring external structural material beyond the shield and barrel. Both a generalized homogenized and a heterogeneous design are provided with corresponding material compositions. The analysis presented in this work is derived from the hot full power model developed based on the heterogeneous layout. Key characteristics are presented in Table 1.

Table 1. Key Characteristics of the ABTR [11]

Reactor power (MWth)	250
Fuel material	U/TRU-Zr10%
Coolant	Sodium
Structural material	HT-9
Fuel slug diameter (cm)	0.7002
Fuel rod diameter (cm)	0.8114
Fuel pin pitch (cm)	0.9134
Active core height (cm)	84.4108
Number of pins per fuel assembly	217
Control rod diameter (cm)	0.9762
Control rod clad diameter (cm)	1.1252
Control rod pitch (cm)	1.2558
Number of rods per control assembly	91
Duct outer flat-to-flat distance (cm)	14.2826
Duct wall thickness (cm)	0.3018
Assembly pitch (cm)	14.685

The core was subdivided into 199 or 253 hexagonal assemblies (depending upon the model), where each assembly uses the same hexagonal duct structure and assembly pitch (Figure 1). The difference in the 199 and 253 assembly models was the outer barrel geometry, discussed in Section 2.2.1. The core consisted of 24 inner fuel assemblies, 30 outer fuel assemblies, 6 fuel test assemblies, 78 reflector assemblies, 48 shield assemblies, 10 control assemblies, and 3 material test assemblies. An additional 54 barrel assemblies are defined in cases where the barrel is approximated as assemblies. The material and fuel test assemblies were modeled as reflector and unique fuel assemblies, respectively. Assemblies shared a similar axial profile, with lower and upper structural homogenization plugs containing reactor components (such as the active fuel region and absorber rod) while sharing duct dimensions into which components were placed. The duct into which reactor components were placed and capped is illustrated in Figure 2.

Figure 3 shows the SCALE models of individual reactor components. Although images are not to scale, the comparison of the triple fuel and reflector assemblies as well as the comparison of the single control and
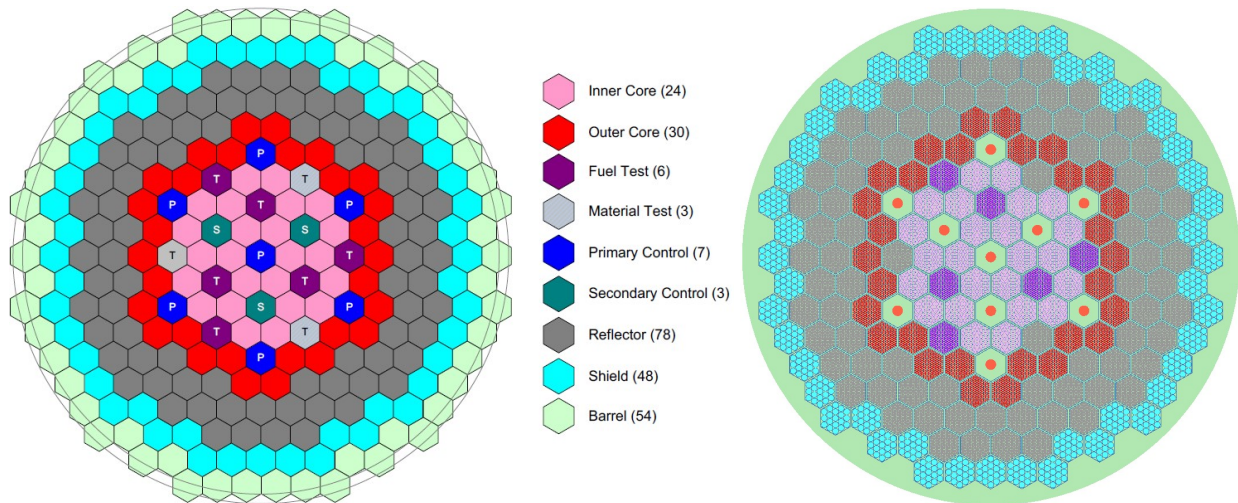
Figure 1. ABTR radial cross section. Comparison of benchmark (left) and SCALE model (right) [11]. Barrel coloring in the SCALE model is sodium coolant surrounded by the cylindrical barrel.

shield assembly demonstrate the identical duct dimensions when scaled to the same degree. Thus, although the duct is scaled appropriately within illustrations of single and triple assembly groupings, the individual size of the components varies. Although most reactor components were effectively arrays of nested cylinders (fuel rods within cladding, boron cylinders within cladding, stainless-steel cylinder reflectors), the control assembly showed a detail worth emphasizing: a follower rod beneath the absorber rods to prevent insertion into the core beyond the active fuel region (see also Section 2.1.2).

2.1.1 Fuel Assembly

There were three types of fuel assemblies of the ABTR in the core, all containing U/TRU-Zr10% fuel with different compositions according to the equilibrium cycle:

- 24 inner core assemblies with a TRU fraction or enrichment of 16.5 wt%,

- 30 outer core assemblies with a TRU fraction or enrichment of 20.7 wt%,

- 6 test fuel assemblies with a TRU fraction or enrichment of 18.7 wt%.

Startup TRU feed that was used to establish the equilibrium ABTR core for this benchmark was weapons-grade plutonium (0.01% ^{242}Pu, 93.81% ^{239}Pu, 5.81% ^{240}Pu, 0.35% ^{241}Pu, 0.02% ^{242}Pu), while the test fuel assemblies used LWR spent fuel in lieu of true test assemblies. LWR spent fuel compositions were based on 10 year–cooled fuel with a discharge burnup of 33 GWd/metric ton initial heavy metal (MTIHM) [6]. In all fuel compositions, the benchmark fission product inventory was simplified into a molybdenum lumped fission product (LFP) equivalent.

Each fuel assembly contained 217 fuel pins arranged in a triangular pitched array, with 17 pins vertex to vertex. Each pin consisted of the fuel slug surrounded by a sodium bond, enclosed in HT-9 cladding. Given operating conditions, fuel swelling was modeled with a taller and thicker fuel slug displacing this sodium bond, resulting in the bond filling a portion of the upper plenum and the fuel slug making direct contact with the cladding. Additionally, the cladding was slightly expanded to represent a thin smear of a simplified wire wrapping around the pin to maintain its position in the array. Below the active fuel region was an HT-9 stainless-steel lower reflector aligned with each individual pin; above the active fuel region was the plenum, containing helium gas and the displaced bond within the HT-9 cladding. Fuel, structure, and coolant temperatures of 855.5 K, 735.5 K, and 705.5 K, respectively, were applied.

4
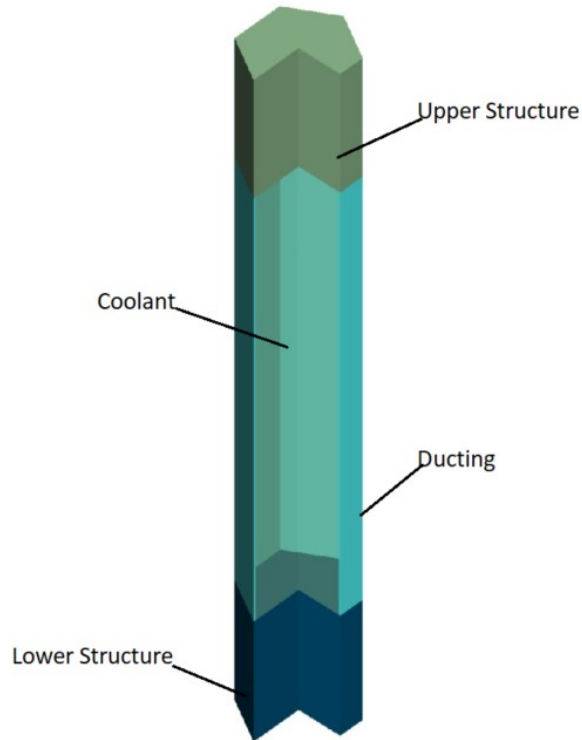
Figure 2. Shared assembly duct and structure. The common ducting and upper and lower structure all non-barrel assemblies are contained within. Not to scale.

2.1.2   Control Assembly

The control assemblies of the ABTR were defined as enclosed bundles of 91 absorber rods arranged in a triangular pitched array, with 11 rods vertex to vertex. Each absorber rod consisted of compacted boron carbide powder, contained within HT-9 cladding. As with the fuel pins, the cladding of the absorber rods was slightly expanded to represent the wire spacer between rods; all dimensions were adjusted for operating temperature expansion. As demonstrated in Figure 3d, the control assembly had an interior duct in addition to the standard assembly duct to channel flow through the absorber rods and maintain integrity by preventing contact between the absorber rods and assembly duct.

The control assembly scheme is split into two banks of control assemblies, with a primary and secondary bank. Functionally, these banks are identical, and no differentiation in the banks is given in the developed model. Control assemblies are withdrawn from the core in the benchmark, with the bottom of the absorber rods aligned with the top of the fuel rods. A cylindrical follower is in place below the absorber rods; a material designation beyond the given atom densities is not provided but bears similarity in composition to the barrel. Although the barrel material is not defined, the design report notes a barrel made of SS-316 steel; thus, the ferrous follower is assumed to consist of SS-316 steel. The positioning of the follower is illustrated in Figure 3. Below the absorber rods and follower is sodium-filled ducting, and as with the fuel assembly, an HT-9 stainless-steel lower reflector. The lower reflector in the control assembly is homogenized to a solid block resting on the lower structure, whereas the fuel reflector is discretely aligned with each fuel pin. Additionally, the lower reflector is two thirds the height of the lower reflector in the fuel assembly. A helium gas plenum is located above the absorber rods, but as with the lower reflector, it is also of reduced height relative to the fuel assembly.
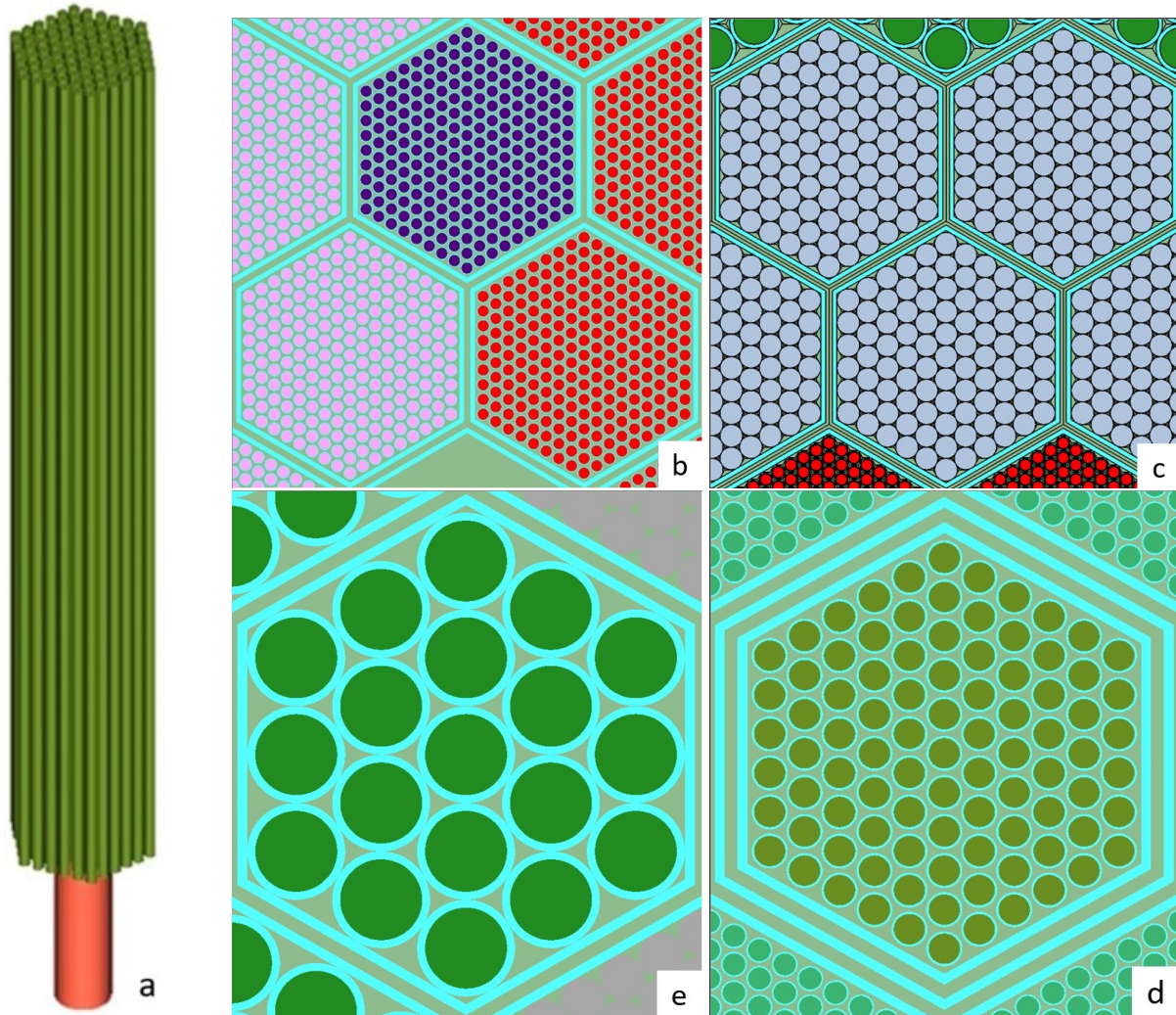
Figure 3. ABTR core assemblies. (a) 3D absorber rods with follower; (b) inner, test, and outer fuel assemblies; (c) reflector assemblies; (d) control assembly; (e) shield assembly. Not to scale.

2.1.3 Reflector Assembly

Reflector assemblies in the ABTR were enclosed bundles of solid HT-9 stainless steel rods. The reflector assembly also consisted of 91 reflector rods, though individually thicker relative to the absorber rods in the control assembly as the reflector rods are not further contained within an interior duct. The rods were arranged in a triangular pitched array with 11 rods vertex to vertex. The rods were not clad, being themselves cladding material. Reflector rods ran the full length within the duct.

2.1.4 Shield Assembly

Shield assemblies in the ABTR were enclosed bundles of boron carbide rods with HT-9 cladding. The shield assembly consisted of 19 boron carbide rods arranged in a triangular pitched array, with 5 rods vertex to vertex. Shield rods ran the full length within the duct.

2.1.5 Barrel Assembly

The barrel assembly is not explicitly defined in the benchmark but is approximated as homogeneous hexagonal blocks containing a homogenized mixture of an undefined ferrous material representing the barrel

material and sodium coolant. The hexagonal block is assumed to confine to the same outer hexagonal dimensions of the standard duct work in other assemblies. Although some simulation codes for SFR analysis are restricted to hexagonal meshes, SCALE does not have this modeling limitation. Therefore, it was possible to explicitly model the outer barrel as cylinder around the core instead of as homogenized hexagonal assembly. As shown in Section 2.2.1, the barrel representation does not have an impact on the eigenvalue.

2.1.6 Full Core

Figure 4 shows a full-core rendering of the developed SCALE model. Minor noted choices were made for visualization of all components. Where possible, color scheming was matched to be consistent with prior figures detailing more specific components. Not detailed in prior figures are the outer barrel encompassing the full core, gas plena at the top of fuel and absorber rods, and the lower reflector in fuel and control assemblies. Figure 1 compares the source benchmark radial layout of assemblies with the SCALE model. The full-core design is just under 2.5 m wide and 3.5 m tall with vacuum boundary conditions. The benchmark specifications provided dimensions, material compositions, and material temperatures at operating conditions. All control assemblies are fully withdrawn.

2.2 MODELING DIFFERENCES AND DISCREPANCIES

During the work, minor inconsistencies were discovered within the ABTR benchmark description. These are discussed here to clarify the assumptions made for the developed SCALE model. A variety of assumptions were made regarding material temperatures, as the given temperatures did not address every material as used to develop a detailed 3D model. These materials include helium, absorber rod and control rod follower, and barrel temperatures.

Helium was not explicitly defined as the fill gas for voided areas in various areas but was noted as a *He bond* in the shield and control assembly definitions. We assumed the fuel pin plenum and any other voided areas were filled with helium gas. As part of the benchmark temperature definitions, the upper plenum was noted to be 510°C, and, as such, the helium was assigned a temperature of 510°C, or 783.15 K. Because helium is a low-density neutronically transparent gas, the effect of incorrectly including helium at an incorrect temperature is negligible. The control rod was assumed to have the temperature of the coolant and reflector materials (432.5°C or 705.65 K) as it is withdrawn from the core, whereas the control rod follower was assumed at the temperature of the lower structure and reflector material (355°C or 628.15 K). Finally, the barrel temperature was not provided and was assumed to be that of the lower structure and reflector material (355°C or 628.15 K). The practical difference in these assumptions is minimal and likely an oversight related to the sister homogenized benchmark configuration with fewer temperatures.

Of final note is the use of the cylindrical barrel. Because this is not a defined feature of the benchmark, its dimensions were assumed; the following section provides a brief sensitivity study of the core to different possible dimensions. The INL report notes the radius used for its calculations: 115 cm [13]. This is reasonable since an inner radius of ~114.1 cm is necessary to fully contain all assemblies at operating temperatures including some spacing for coolant flow.

2.2.1 Barrel Sensitivity

The benchmark was designed with deterministic solvers in mind that are limited to hexagonal meshes. In this approach, the barrel was implemented as a ring of hexagonal barrel assemblies that included a mixture of barrel and coolant material. SCALE has the capability of modeling the barrel either as a ring of hexagonal barrel assemblies or as a cylindrical encasement of the core. A sensitivity study of different modeling approaches for the barrel was performed, and three states were investigated: the barrel assembly model as given in the benchmark; a cylindrical barrel with an inner and outer radius of 115 and 117.54 cm,

Core Radius
(115 cm)

Upper Plenum
& Control Rods
(115 cm)

Active Core
(85 cm)

Lower Reflector
(60 cm)

Lower Structure
(50 cm)
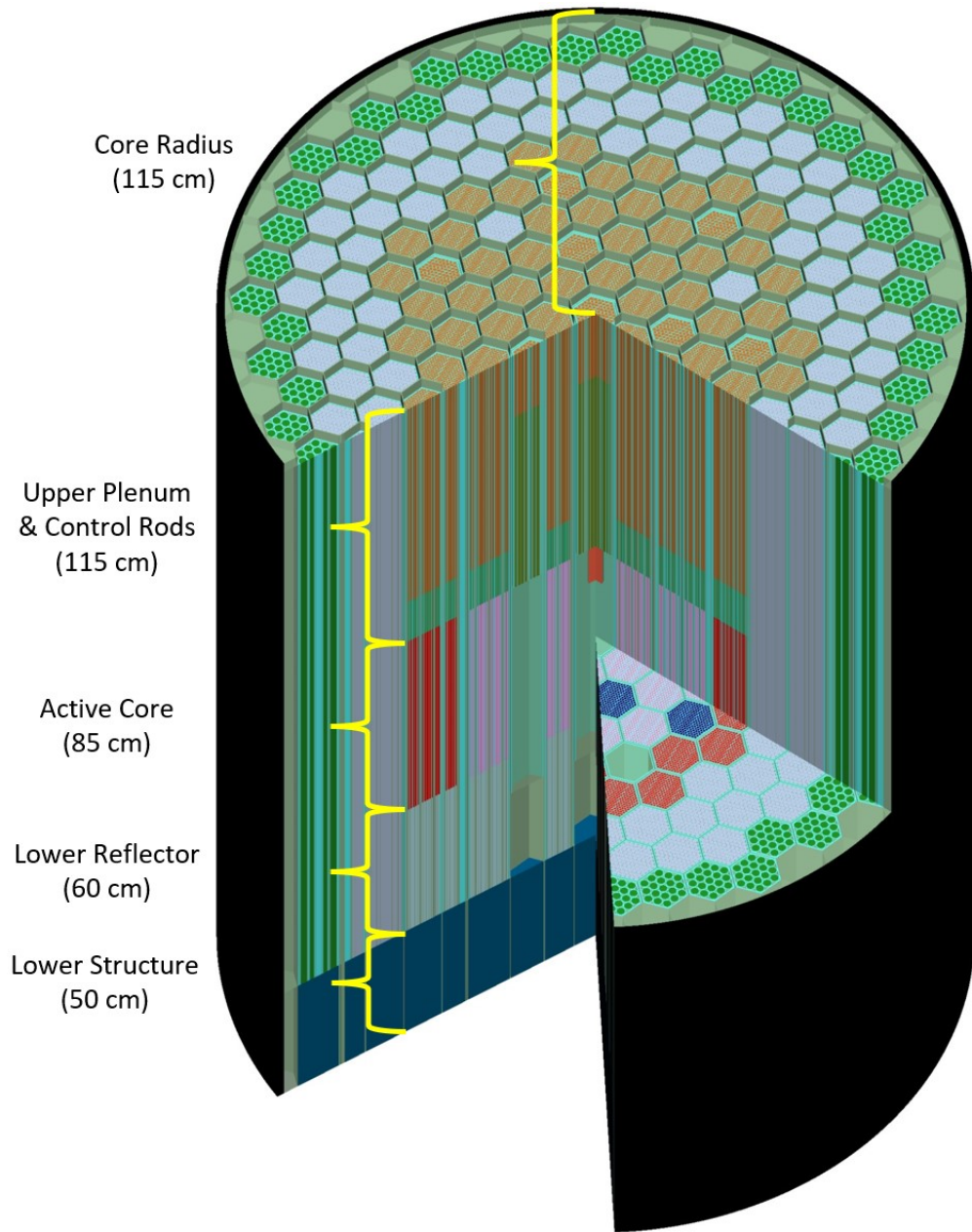
Figure 4. SCALE full-core model. Upper structure not rendered to provide more detailed view from the top. Coolant rendered with reduced opacity, and provided region dimensions are rounded to the nearest 5 cm.

respectively, as used in the INL Serpent model [13]; and a cylindrical barrel with an inner and outer radius of 114.413 and 116.973 cm, respectively, derived from the thermal expansion of the barrel at inlet coolant temperature (Figure 5). All three configurations are shown to be statistically equivalent in Table 2. The 115 cm cylinder configuration is the selected configuration for all other analysis presented in this report.

Table 2. Core barrel shape sensitivity

Case	k_{eff}	Difference (pcm)
Barrel assemblies	1.03025 ± 0.00004	(ref)
115 cm cylinder	1.03017 ± 0.00003	−9 ± 5
114.413 cm cylinder	1.03014 ± 0.00004	−11 ± 5
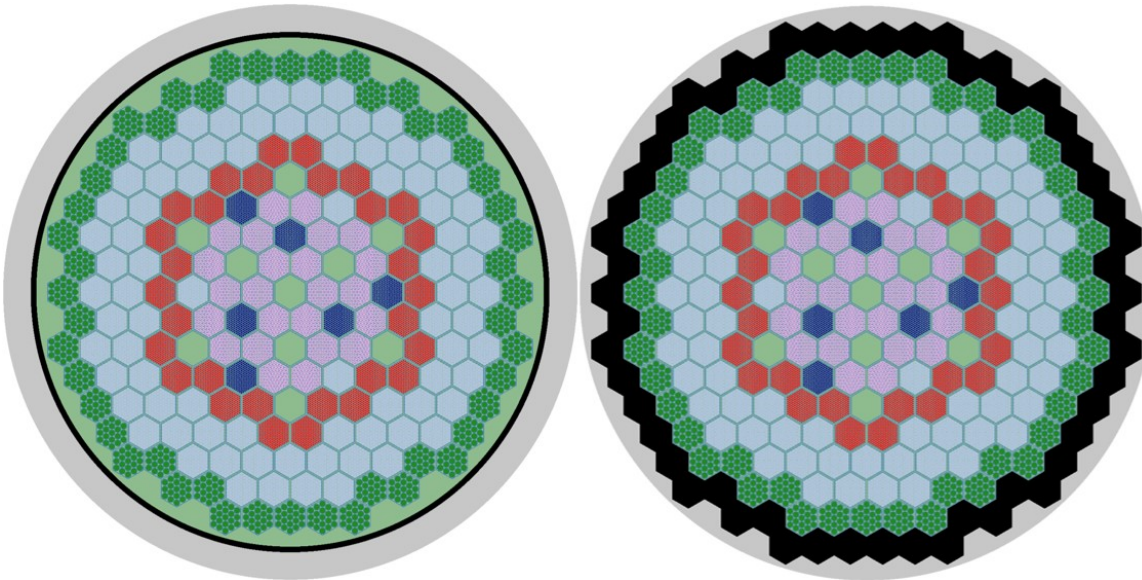
Figure 5. Barrel definitions. Use of cylindrical and assembly barrel design choice. Outer grey represents void.

2.3 PARAMETER SETTINGS FOR ANALYSES

All calculations were performed with SCALE 6.3.0 on an ORNL Linux cluster. However, for only the EOEC prompt fission neutron spectrum (PFNS) calculation for determining the effective delayed neutron fraction, a development version of SCALE 7.0 was used to avoid an issue with data discrepancies for certain fissionable materials causing memory faults in prompt-only calculations in 6.3.0. For reactivity calculations, SCALE's Criticality Safety Analysis Sequence (CSAS) was used in combination with the 3D Monte Carlo code KENO-VI. The calculation used 4,000 active generations with 100,000 neutrons per generation, yielding final k_{eff} uncertainties below 4 percent mille (pcm). For depletion calculations, SCALE's TRITON sequence was employed, which automates the execution of the neutron transport solver (in this case, KENO-VI) and the depletion/decay solver ORIGEN. Six depletion intervals were used across the 4 month cycle of the ABTR operating at 61.777 MW/MTIHM. Although ORIGEN tracks >2,000 nuclides in the depleted mixtures, only a subset is considered during the individual neutron transport calculation to limit computation time (six depletion intervals require seven neutron transport calculations). TRITON's default subset *addnux=2* was chosen, which includes 94 relevant nuclides in addition to the initial fuel composition and is sufficient for an accurate calculation of the neutron flux. In addition to fuel compositions at EOEC, TRITON was used to

analyze axial and radial power profiles of the core through the evaluation of mixture-specific powers. Since TRITON does not provide estimates of the Monte Carlo statistical uncertainties in the mixture-specific powers, Section 5.2.4 demonstrates how these uncertainties are derived through multiple calculations with different random number seeds for the Monte Carlo neutron transport calculations. All CSAS and TRITON calculations were performed with ENDF/B-VII.1 cross section libraries; only one calculation was performed with the ENDF/B-VIII.0 cross section library to determine the impact of the library choice on k_{eff}. CSAS and TRITON used the Monte Carlo code KENO-VI in continuous energy (CE) mode.

3. SCALE MODEL VERIFICATION

To confirm the accuracy of the SCALE/CSAS BOEC input representing the benchmark model, comparisons of SCALE results with published results were performed for k_{eff} and β_{eff}.

3.1 EIGENVALUE

Although the benchmark specifications did not provide reference k_{eff} results, a recent INL report using the same benchmark provides results obtained with the Serpent code [13]. This independently produced model using a different code provides a basis for verification of the SCALE input, both codes simulating an identical source benchmark with identical source nuclear data—the ENDF/B-VII.1 cross-section library. Results of the Serpent and SCALE calculations are presented in Table 3. Although the results are statistically distinguishable with a difference of 37 ± 4 pcm, for independent codes and input files, this is considered excellent agreement.

Table 3. BOEC eigenvalue comparison between SCALE and Serpent

Code	XS Library	k_{eff}	Difference (pcm)
Serpent [13]	ENDF/B-VII.1	1.03055 ± 0.00002	(ref)
SCALE	ENDF/B-VII.1	1.03019 ± 0.00004	−37 ± 4

3.2 DELAYED NEUTRON FRACTION

In addition to k_{eff}, β_{eff} at BOEC was reported in both the initial design report [6] and the INL report [13]. Both sources note a calculated β_{eff} of 0.0033, or 330 pcm, with no cited uncertainties. β_{eff} can be calculated with the Bretscher prompt k_{eff} ratio defined in Eq. (1) [5]. This requires a calculation of k_{eff} with the total neutron spectrum (total ν based on both the delayed and the prompt ν; this is the default) and a second calculation in which only the PFNS is used (prompt ν). SCALE can run calculations with the prompt ν by enabling the keyword *pnu=yes* in the *parameter* block. Using this approach, a β_{eff} of 331 ± 5 pcm is obtained, which is in excellent agreement with the reported results (Table 4). Whereas individual k_{eff} calculations and other parameters of interest are heavily stress tested in SCALE criticality safety, reactor physics, and shielding applications, β_{eff} has not yet not been included in published validation reports to validate the PFNS implementation. Future validation reports will include validation of available β_{eff} data.

$$\beta_{eff} = 1 - \frac{k_p}{k}. \tag{1}$$

Table 4. BOEC β_{eff} verification

Code	XS Library	β_{eff} (pcm)
DIF3D [6]	ENDF/B-V.2	330
Serpent [13]	ENDF/B-VII.1	330
SCALE	ENDF/B-VII.1	331 ± 5

4. CSAS FULL-CORE BOEC ANALYSIS

This section presents the main results for eigenvalue, neutron flux distribution, and reactivity coefficients of the ABTR core at BOEC.

4.1 EIGENVALUE

The effect of the nuclear data library was assessed by re-running the nominal k_{eff} calculation with the ENDF/B-VIII.0 nuclear data library. An effect of only 133 pcm was observed (Table 5), likely caused by updates in relevant actinide cross sections such as fission and neutron multiplicity of the fissile nuclides. Based on previous studies [2], the effect of nuclear data library changes is expected to be negligible for reactivity coefficients. Therefore, all other reactivity calculations presented in this section were performed only with ENDF/B-VII.1.

Table 5. Effect of the nuclear data library on the BOEC eigenvalue

XS Library	k_{eff}	Difference (pcm)
ENDF/B-VII.1	1.03019 ± 0.00004	(ref)
ENDF/B-VIII.0	1.03152 ± 0.00004	133 ± 4

4.2 FLUX DISTRIBUTION

Figure 6 shows the neutron flux per unit lethargy at several regions throughout the BOEC core. Despite higher concentrations of ^{239}Pu in the outer core (and nearly equivalent ^{235}U concentrations), the inner core has harder neutron spectrum due to radial neutron leakage and lower energy of reflected neutrons. Within the outer reflectors, there is relatively minor softening of the spectrum, as expected in a fast reactor.

Figure 7 shows the flux per unit lethargy at several axial locations: zone 1 is at the bottom of the active core and subsequent zones are at axial positions approximately every 20 cm up to the active core height of ~85 cm. The flux of the inner assembly that was also shown in Figure 6 is displayed. The flux spectrum and magnitude is similar in zones 2–4. The bottom and top zones 1 and 5, respectively, have lower flux magnitudes due to axial leakage with zone 1 slightly higher than 5 due to the presence of a lower axial reflector.

Figure 8 shows an XZ cross-sectional heat map of the total neutron flux throughout the core. Note that the units are based on normalization of the neutron flux to the fission neutron and the mesh voxel volume and do not correspond to absolute flux units.
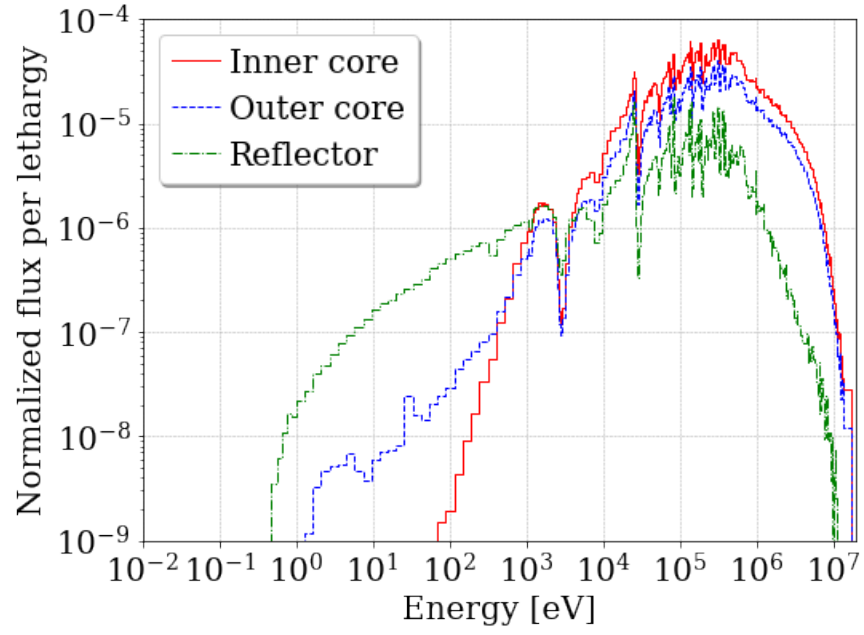
Figure 6. BOEC neutron flux spectrum at different radial positions.
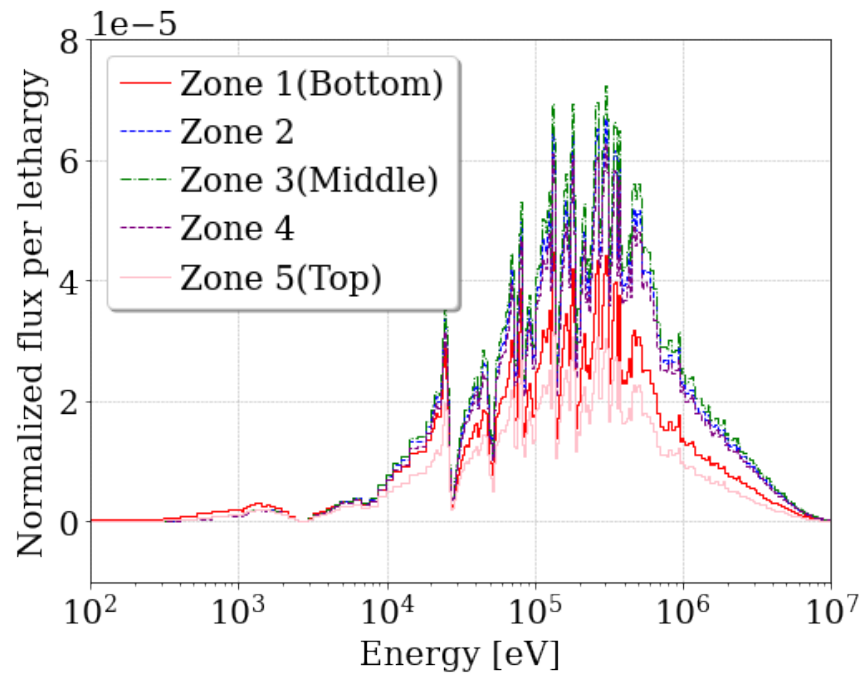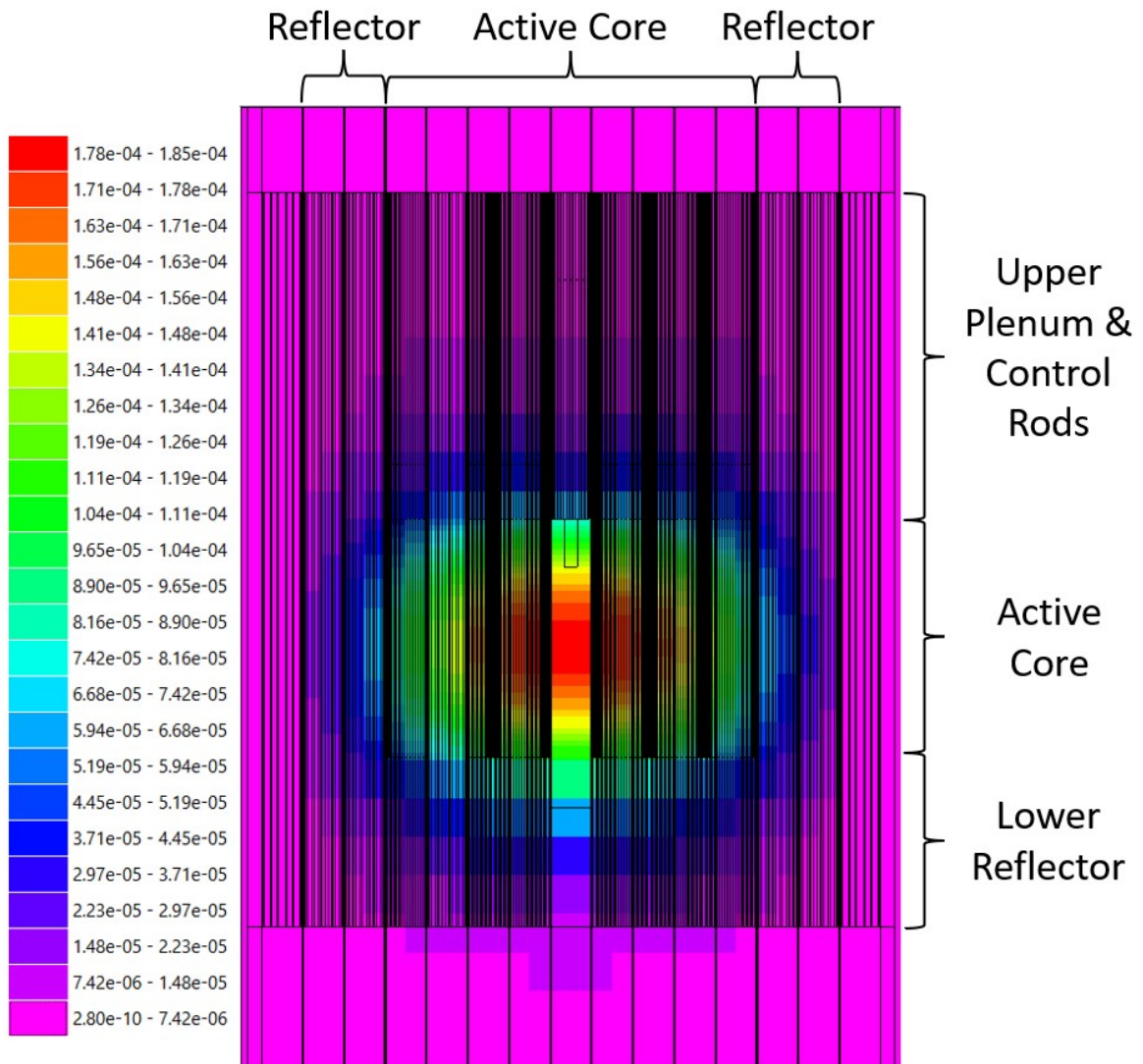

Figure 7. BOEC neutron flux spectrum at different axial positions through the active core.

Figure 8. BOEC neutron flux.

4.3 REACTIVITY FEEDBACK

A series of important reactivity feedback coefficients were calculated at BOEC. These included density and temperature coefficients, as well as thermal expansion coefficients. The thermally expanded dimensions are determined using

$$L_f = L_i + L_i \cdot \alpha_{avg} \cdot \Delta T, \tag{2}$$

where L_f and L_i are the final and initial dimensions, respectively, α_{avg} is the mean thermal expansion coefficient, and ΔT is the temperature difference across which the expansion occurs. Descriptions of how each of these coefficients were calculated are given in the following sections. Table 6 shows the assumed thermal expansion coefficients and corresponding temperature perturbations used.

Table 6. Summary of assumed thermal expansion coefficients

	U/TRU-Zr	SS-316	HT-9	Sodium
α_{avg} (1/K)	$1.74 \cdot 10^{-5}$ [9]	$1.79 \cdot 10^{-5}$ [20]	$1.39 \cdot 10^{-5}$ [22]	$2.71 \cdot 10^{-4}$ [7]
ΔT (K)	574	336	720	370

The reactivity coefficients are calculated by performing eigenvalue calculations for the nominal reference model and for a model with perturbed input parameters (perturbed temperature, density, or geometry). The coefficients are determined by dividing the reactivity difference between the perturbed and reference calculation by the temperature difference corresponding to the perturbation:

$$C_R = \frac{\Delta \rho}{\Delta T} = \frac{\frac{1}{k_{nominal}} - \frac{1}{k_{perturbed}}}{\Delta T}, \tag{3}$$

In the case of temperature feedback coefficients, the temperature difference is directly applied. In the case of density or geometry feedback coefficients, the temperature differences that would cause the applied perturbation is used.

To be consistent with common SFR literature and to consider how MELCOR's uses reactivity coefficients, the unit used for reactivity in this section is dollar ($), defined as $1.0\ \$ = \beta_{eff}$. For small reactivity changes, cent (¢) is convenient, $1\$ = 100¢$. For the calculation of the reactivity coefficient in dollars consequently follows:

$$C_{R,\$} = \frac{C_R}{\beta_{eff}} = \frac{\Delta \rho}{\Delta T \cdot \beta_{eff}}, \tag{4}$$

Calculations in this section use $\beta_{eff} = 0.00331 \pm 0.00005$ as calculated in Section 3.2. To determine the statistical uncertainty of the coefficients $C_{R,\$}$, the statistical uncertainties of the eigenvalues and of β_{eff} from the Monte Carlo calculation are propagated using standard first order error propagation.

4.3.1 Axial Fuel Expansion Coefficient

Matching the methodology used in the design report [6], the axial thermal expansion coefficient assumes a hypothetical 1% expansion in only the axial direction. With a nominal active fuel height of 84.4108 cm, the fuel was therefore further expanded by 0.8441 cm. As a result, the fuel density was reduced by 1% so that the total fuel mass remained constant. Because the fuel pins are located directly on top of the lower reflector pins, the expansion occurs upward into the upper plenum. Since the control rods are located directly above

the fuel region, the axial fuel expansion implies a small net control rod insertion, which enhances the negative reactivity response.

Equation (2) is used to determine the temperature change corresponding to the 1% expansion. The average thermal expansion coefficient for U-Pu-Zr alloys is $1.74 \cdot 10^{-5}$/K in Table 20 in Section 2.4.1.4.1 of [9]. This is considered an adequate coefficient for the U/TRU-Zr fuel as only minor differences are expected from the addition of other actinides in the fuel. Using this coefficient, the 1% axial fuel expansion was found to correspond to a 574 K temperature increase. Using the eigenvalues for both the expanded and nominal models, along with this calculated temperature range, an axial fuel expansion coefficient of -0.146 ¢/K was calculated.

4.3.2 Radial Grid Plate Expansion Coefficient

According to the ABTR design report [6], the radial thermal expansion represents the reactivity effects of uniform, radial thermal expansion of the SS-316 grid plate, which is governed solely by the coolant inlet temperature. As the grid plate expands radially, the hexagonal core lattice pitch, and therefore the distance between the fuel assemblies, increases. This is not to be confused with radial fuel thermal expansion; the fuel dimensions remain constant and only the assembly pitch changes.

The cold core inlet temperature is assumed to be room temperature (293 K), and the expanded temperature at operating conditions is 628 K. Using the thermal expansion coefficient for SS-316 of $1.79 \cdot 10^{-5}$/K from Table 1.1 in Section 1.2.1.1 in Appendix C of [20] in Eq. (2) leads to a center-to-flat radius increase of 0.0440 cm. While this expansion of 0.0440 cm is corresponding to the change from cold to hot conditions, a 0.0440 cm expansion is applied in these simulations to the hot core, leading to a radial expansion coefficient of -0.334 ¢/K. The grid expansion causes an increase in sodium in the core and an increase of the core volume, which causes an increase of leakage, resulting in an overall negative reactivity effect.

4.3.3 Fuel Density Coefficient

Similarly to the axial fuel expansion coefficient, the fuel density was reduced by 1%, but the fuel dimensions were not changed. As a result, the fuel mass of the reactor was not conserved in the perturbed reactor model. Although this is not physical, this calculation was performed consistent with the design report. A fuel density coefficient of -0.243 ¢/K was calculated, which is significantly larger than the axial fuel expansion coefficient of -0.141 ¢/K calculated in Section 4.3.1. This result makes sense given that the fuel density coefficient includes the effect of a perturbed fuel mass.

4.3.4 Structure Density Coefficient

The structure density coefficient was calculated by adjusting the density for all structural components composed of HT-9 without changing the geometry. The densities of the fuel cladding, assembly ducts, outer reflector, lower reflector, upper and lower structure, control rod followers, and core barrel were all reduced by 1%. The thermal expansion coefficient used for HT-9 was $1.39 \cdot 10^{-5}$/K, which was taken from [22]. This thermal expansion coefficient implies that a temperature difference of 720 K would cause the density of the structure to change by 1% (assuming spatial expansion to cause the density decrease, although only density decrease is considered here). Using this coefficient and temperature along with Eq. (2) yields a structure density coefficient of -0.011 ¢/K. This low reactivity coefficient is due to the fact that these structural components are not neutronically significant.

4.3.5 Sodium Void Worth

The sodium void worth was calculated using the same methodology described in the ABTR design report [6]. The sodium was voided inside the assembly duct both in the active fuel region and above, but it was left

unchanged below the active fuel. The bonded sodium within the fuel clad was left in place, as well as the sodium within the control assembly ducts, reflector ducts, shielding ducts, and the channels between all assemblies. Comparing the eigenvalues between the nominal and voided models yielded a sodium void worth of −0.451\$. The sodium void worth is mainly a result of (1) hardening of the neutron spectrum because of less moderation of the neutrons through the coolant which leads to an increased fission-to-capture ratio and therefore positive reactivity insertion and (2) increased leakage because of fewer interactions of the neutrons with the coolant (or none in the case of voiding) and therefore negative reactivity insertion. A decrease of parasitic neutron capture by the coolant provides an additional minor positive reactivity insertion. For the ABTR, the leakage compensates for the spectrum hardening effect, yielding an overall negative sodium void coefficient.

This sodium void worth might differ from other values reported in the literature. Modeling differences such as the selection of voided regions and heterogeneous vs. homogeneous assembly modeling approaches are likely the source of these discrepancies. The SCALE model used in this work was modeled based on the heterogeneous benchmark specifications. According to [22], homogeneous calculations tend to overestimate the value of the sodium void worth by 200 to 300 pcm. With a β_{eff} of 0.0033, these are differences of ~0.60–0.90\$. Additionally, the calculations performed here applied the ENDF/B-VII.1 cross section library, whereas other studies in the literature used much older nuclear data libraries. According to [31], for both homogeneous and heterogeneous models, older libraries, like ENDF/B-V, can lead to a positive sodium void worth; conversely, newer ENDF/B-VI and ENDF/B-VII.0 libraries can result in a negative worth for the same configuration.

It is interesting to note that the void worth is spatially dependent, and the overall void worth typically increases with reactor size. The spectral effect dominates in the central part of the core, but the leakage component is high in the peripheral regions. Because fractionally fewer assemblies are located toward the periphery in a large core compared to a small core, voiding has a relatively reduced negative leakage reactivity effect in the larger core. In contrast, the spectral effect is much larger in larger cores, which can result in overall positive sodium void worth. This effect is considered in modern SFR designs that aim to maximize leakage effects: for example, by decreasing the height-to-diameter ratio and introducing an upper sodium plenum [27].

4.3.6   Sodium Density Coefficient

The sodium density coefficient was calculated by reducing the sodium density by 10%. All flowing sodium in the model was perturbed: the sodium in all ducts and channels as well as the sodium in the homogenized lower structure and lower reflector regions. Using a thermal expansion coefficient of $2.71 \cdot 10^{-4}$/K based on Table 1.3-4 of [7] in Eq. (2), the sodium temperature difference that would cause a 10% density change was determined to be 370 K. The sodium density coefficient was calculated to be −0.114 ¢/K. This negative value follows the sodium void worth calculated in Section 4.3.5.

4.3.7   Doppler Coefficient

Because the fuel Doppler reactivity does not follow a linear function of the fuel temperature, the ABTR's reactivity was calculated at multiple fuel temperatures (Figure 9): the nominal 855.65 K, nominal ± 50 K, nominal ± 100 K, nominal + 200 K, 2× nominal, cold shutdown temperature of 478.15 K, and hot zero power temperature of 628.15 K. The cold shutdown and hot zero power temperatures were taken from [6]. The reactivity response as a function of fuel temperature is expected to be logarithmic [27], so a logarithmic fit was imposed on the data with a coefficient of determination greater than 0.995. The Doppler coefficient was calculated at the nominal fuel temperature (855.65 K) by taking the derivative, that is, the gradient, of the logarithmic fit at this temperature. A negative coefficient of −0.117 ¢/K was obtained, as expected due to the broadening of resonances at higher temperatures. Note that a linear fit between two points (nominal and

twice operating temperature) would have resulted in a coefficient of −0.079 ¢/K, and a linear fit over all nine points would have resulted in a coefficient of −0.098 ¢/K. Both results are significantly different from the logarithmic fit and therefore indicate that linear fits are inadequate for this type of analysis.
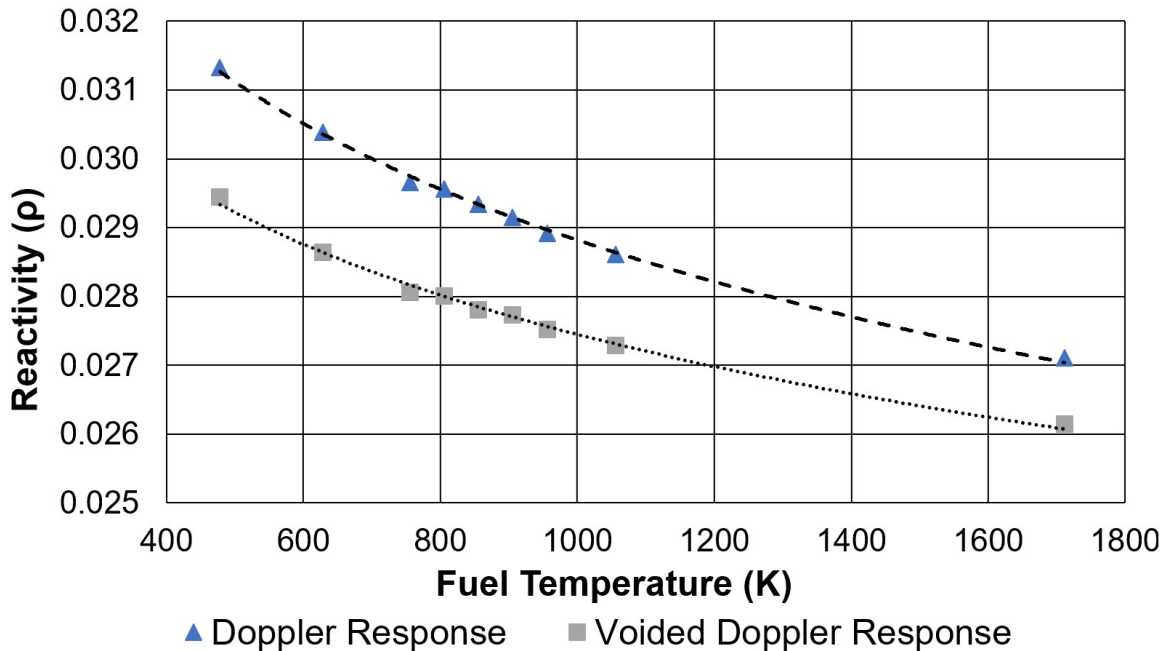
Figure 9. Fuel temperature dependence of nominal and voided reactivity. Uncertainties in both reactivity responses are below 4 pcm and not visible on the plot.

4.3.8 Sodium-voided Doppler Coefficient

Calculating the sodium-voided Doppler coefficient follows the same strategy used to calculate the Doppler coefficient in Section 4.3.7. The reactivity was again calculated at nine temperature points, but this time with the ABTR model voided of sodium, per Section 4.3.5—that is, without sodium within the fuel assembly duct in the active fuel region and above. The data points, log fit, and error bars are shown in Figure 9. The voided Doppler coefficient of −0.09 ¢/K was obtained at the nominal fuel temperature . As seen in [6], the voided Doppler coefficient is slightly less negative because the hardened neutron spectrum reduces the fraction of neutrons interacting with resonances and thus being affected by temperature changes. Note that using a linear fit between two points (nominal and twice operating temperature) would have resulted in a coefficient of −0.061 ¢/K, and a linear fit over all nine points would have resulted in a coefficient of −0.075 ¢/K. As for the nominal Doppler coefficient, both results are significantly different from the logarithmic fit and therefore indicate that linear fits are not adequate for this type of analysis.

4.3.9 Summary

All calculated reactivity feedback effects are listed in Table 7 with their statistical uncertainties propagated from the individual Monte Carlo calculation results. All temperature coefficients are negative, indicating that increasing temperature reduces the overall reactivity of the core. Sodium void is also a clear negative reactivity effect. Discrepancies between these values and others presented in the literature may be due to the applied nuclear data library, the modeling choice with homogenized or heterogeneous assemblies, and/or details in the reactivity coefficient calculation, such as the type of fit or the value of β_{eff}. Additionally, the resolution of small reactivity differences can be challenging in Monte Carlo methods, as the relative

statistical uncertainty of these differences, propagated from the individual k_{eff} calculations, can be large. Therefore, the calculation of the reactivity coefficients presented herein is described in detail to allow for the best possible understanding and replication.

Table 7. Summary of full-core reactivity feedback effects

Feedback effect	Value ± Std. Dev.
Axial fuel expansion coefficient (¢/K)	−0.146 ± 0.003
Radial grid plate expansion coefficient (¢/K)	−0.334 ± 0.007
Fuel density coefficient (¢/K)	−0.243 ± 0.004
Structure density coefficient (¢/K)	−0.011 ± 0.002
Sodium void worth ($)	−0.451 ± 0.016
Sodium density coefficient (¢/K)	−0.114 ± 0.004
Doppler coefficient (¢/K)	−0.117 ± 0.003
Sodium-voided doppler coefficient (¢/K)	−0.090 ± 0.003

4.4 CONTROL ASSEMBLY WORTH

Control assemblies were inserted into the core to measure the eigenvalue response to various assembly insertions. An assembly worth was determined by inserting the noted control assemblies into the core and calculating the eigenvalue response (e.g., center assembly worth is calculated by calculating the eigenvalue difference between the nominal core and a core with only the inserted center assembly). The primary bank of control assemblies consists of the center assembly as well as the six assemblies in the fifth ring. The secondary bank of control assemblies consists of three assemblies in the third ring. All control assemblies are identical. To represent the insertion of the control assembly, the bundle of absorber rods and the control rod follower were lowered into the core such that the bottom of the follower rested just above the control assembly lower reflector and the absorber rods aligned vertically with the fuel rods (see Figure 10 for an example.) The components were lowered 85.5 cm relative to the uninserted position, though this positioning is not explicitly given as the point of maximum or reasonable insertion. Table 8 presents the calculated BOEC insertion worths. Control assembly worths are presented as positive but reflect negative reactivity insertions.

Additionally, Table 8 provides results from the original design report [6] using the DIF3D code and ENDF/B-V.2 cross section library. SCALE results are calculated direct eigenvalue difference (instead of reactivity differences) to be consistent with the DIF3D approach taken in the design report [6]. There is excellent agreement between the results despite the difference in cross section library and methods used. Control assembly insertion reflects a large perturbation of the system with significant global effects, unlike some of the reactivity coefficient perturbations. For strong absorbers, the strong reactivity impact overshadows the effect of the differences in the underlying nuclear data. Furthermore, the effect of cross section changes on eigenvalue differences was already shown to be smaller than that for k_{eff} itself [2]. When analyzing the difference between DIF3D and SCALE as a function of EALF (SCALE reports EALF by default in these calculations), a slight trend of an increasing difference with increasing EALF can be observed (Figure 11). With all primary assemblies inserted the difference in worth is approximately 7%.
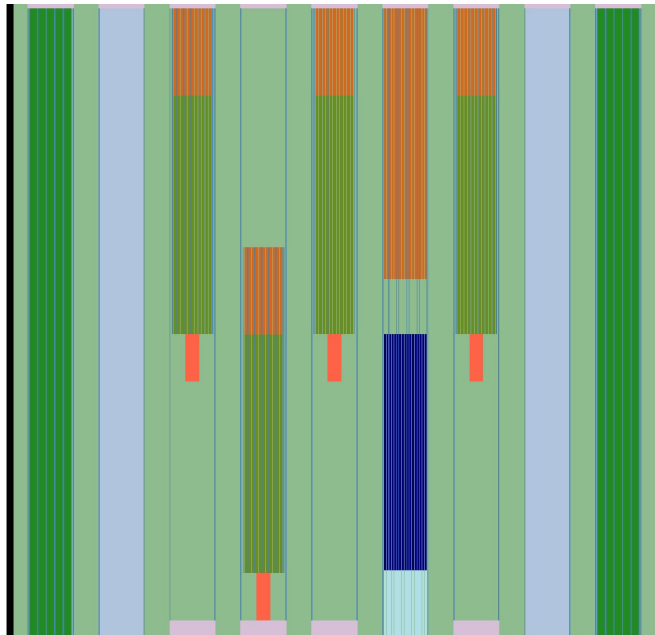
Figure 10. Control assembly insertion (green), based on a Y-Z cutplane through the center of the core.
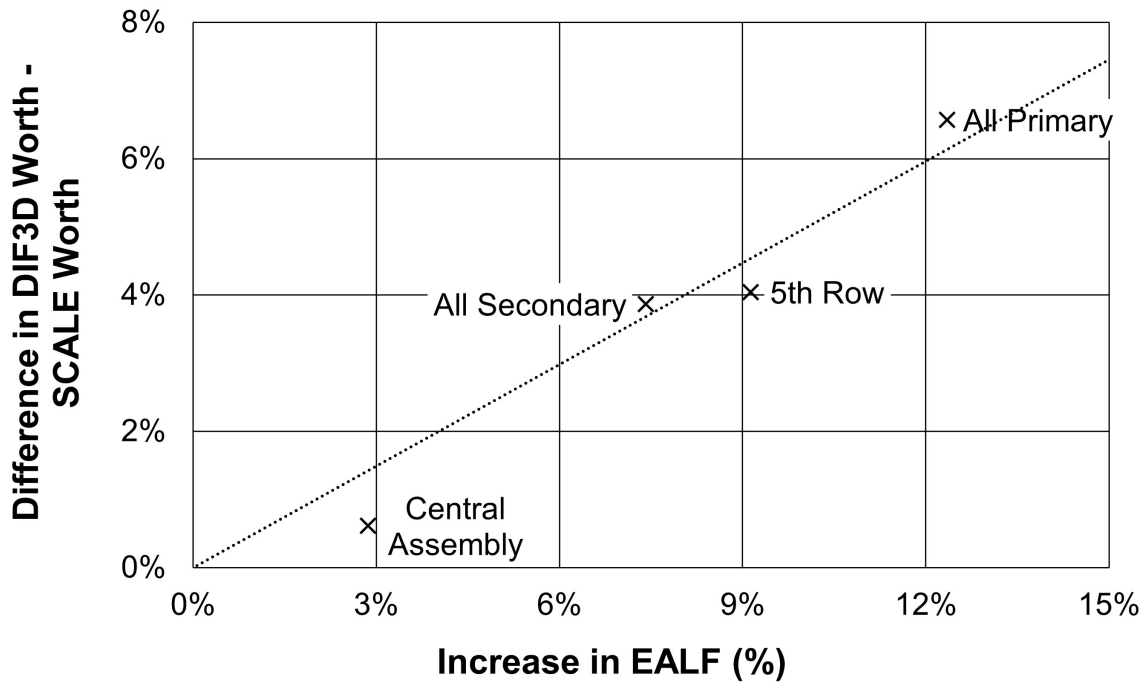
Figure 11. Increased discrepancy between DIF3D and SCALE control worths as a function of EALF (increases with spectral hardening).

Table 8. Control assembly worths at BOEC

	Inserted control assemblies	DIF3D worth ($) [6]	SCALE worth ($)
Primary bank			
- Central assembly	1	6.53	6.49 ± 0.10
- Fifth row	6	15.95	15.33 ± 0.23
- All primary	7	23.52	22.07 ± 0.33
Secondary bank			
- All secondary	3	16.38	15.77 ± 0.23

5. TRITON FULL-CORE DEPLETION AND EOEC ANALYSIS

Accident simulations must be initiated with representative fuel inventory. For this purpose the ABTR BOEC core was depleted for one 4 month cycle to EOEC. While more than 2,000 nuclides are tracked during SCALE's depletion calculation to arrive at a detailed EOEC nuclide vector, the fission products in the BOEC fuel were approximated as LFP according to the benchmark specification. This is expected to introduce a small bias to the fission product inventory at EOEC. The following presents an analysis of the decay heat after shutdown, radial and axial power profiles, and local sodium void effects on reactivity and power for the EOEC core.

5.1 DECAY HEAT SUMMARY

The decay heat of the EOEC core[1] is one of the main drivers of a severe accident and is detailed in the severe accident analyses from the SNL MELCOR report [16]. Table 9 details the top 10 nuclides and their respective contributions to decay heat in the first 30 seconds, the first 30 days, and beyond. During this analysis the highlighted nuclides ^{104}Tc and ^{242}Cm were noted to have larger than average differences in contribution to decay heat compared to the LWR for certain respective time ranges. This is explored further in the time-dependent behavior shown in Figure 12.

Table 9. EOEC ABTR decay heat contributors for various decay time ranges

|	$0 < t < 30$ s		30 s $< t < 30$ days		30 days $< t < 100$ years	
	Nuclide	Contribution	Nuclide	Contribution	Nuclide	Contribution
1	Tc-104	2.32%	Np-239	4.87%	Nb-95	15.91%
2	U-239	2.30%	La-140	4.03%	Rh-106	14.83%
3	I-134	2.17%	I-134	3.53%	Pr-144	11.80%
4	Np-239	2.02%	I-132	3.37%	Cm-242	11.77%
5	Cs-138	1.98%	U-239	3.02%	Zr-95	11.64%
6	Nb-100	1.66%	Cs-138	3.00%	Ru-103	7.30%
7	Tc-106	1.62%	Tc-104	3.00%	La-140	4.87%
8	Cs-140	1.48%	La-142	2.30%	Y-91	4.19%
9	La-144	1.43%	I-135	2.22%	Sr-89	2.55%
10	La-140	1.43%	I-133	1.43%	Pu-239	2.31%

Figure 12a shows decay heat as a percentage of operating full power following shutdown for the ABTR at the end of the 4 month cycle compared with that of a pressurized water reactor (PWR) at the end of a cycle. The PWR data is approximated using SCALE/ORIGAMI with three batches of Westinghouse 17×17 fuel assemblies at 20, 40, and 60 GWd/MTIHM burnup. The decay heat of the ABTR starts with a slightly higher initial decay heat compared to the PWR but quickly assumes an identical shape.

As an example of the capabilities to determine nuclide-specific decay heat contributions, Figure 12b shows the decay heat of the top 10 contributing nuclides over the first 100 days, Figure 12c shows a shorter time

---

[1]TRITON full-core depletion calculations resulted in fuel inventory for ~2000 nuclides at EOEC, stored in binary ORIGEN concentration (*f71*) file. Used in previous non-LWR analysis as a part of the NRC task, the SCALE OBIWAN formatting utility allows for the conversion of these inventories into a JSON-formatted inventory interface file (*ii.json*), which can then be converted via a Python script into a MELCOR *DCH* decay heat input file. A core-average *ii.json* was generated and converted into a *DCH* file that was provided to the MELCOR team. All relevant files and scripts are available on the public Gitlab repository associated with the overarching NRC project and this ABTR analysis at https://code.ornl.gov/scale/analysis/non-lwr-models-vol3.
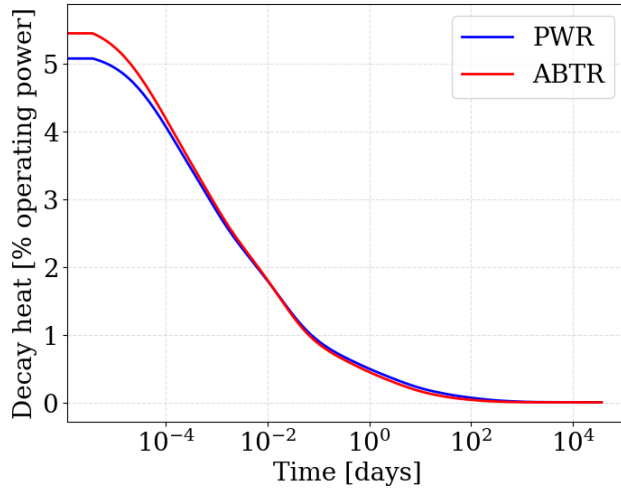
(a) **Decay heat of the ABTR following shutdown compared with a reference PWR.**
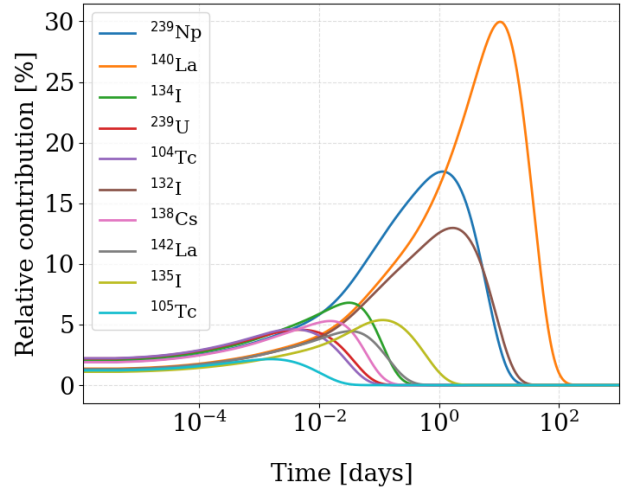
(b) **Top 10 nuclides contributing to ABTR decay heat for the first 100 days.**
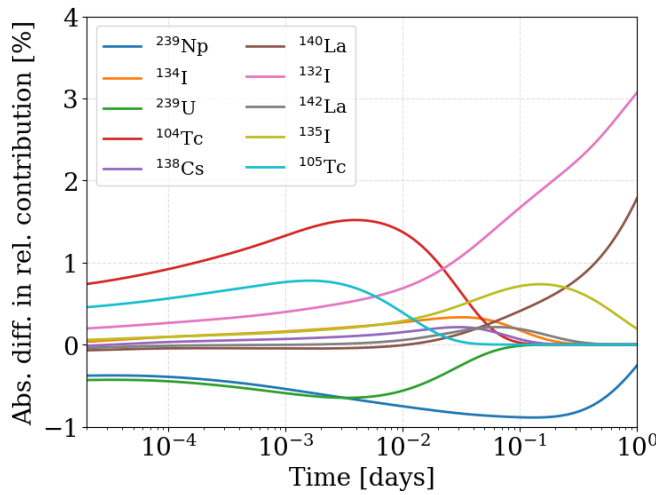
(c) **Difference in decay heat contribution between the ABTR and a reference PWR at short times.**
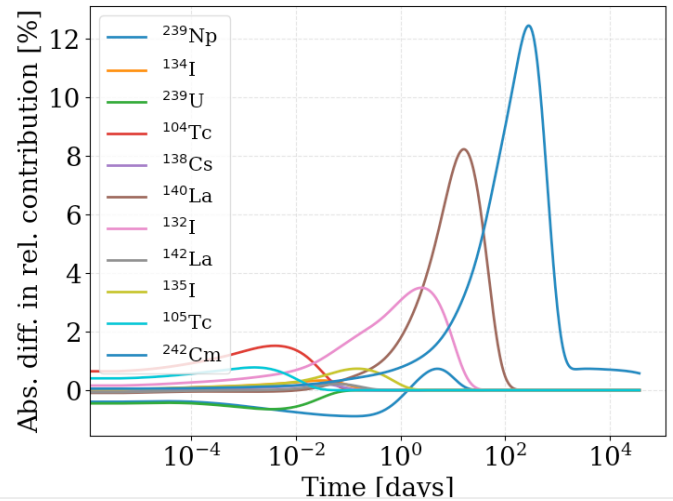
(d) **Difference in decay heat contributions between the ABTR and a reference PWR at long times.**

Figure 12. **Decay heat, major contributing nuclides, and comparisons with other reactors.**

scale where [104]Tc dominates the *difference between ABTR and PWR*, and Figure 12d shows the longer time scale where [242]Cm dominates the *difference*.

[104]Tc has a half-life of ~18 min and has a larger contribution in the ABTR for the following reasons.

1. The use of the LFP at BOEC leads to a significant amount of molybdenum (Z=42) at EOEC which might be overestimated compared to a model that does not include a LFP model. Additionally, zirconium concentrations are elevated with U/TRU-Zr10% fuel. Both [104]Mo and [104]Zr are parent nuclides of [104]Tc and are potential activation products.

2. Production from [239]Pu due to the ABTR having significantly more plutonium relative to LWRs and even other non-LWRs. The [104]Tc fission product yield of ^{239}Pu at 2 MeV is an order of magnitude higher than ^{235}U, as shown in Figure 13 from the National Nuclear Data Center (NNDC) [14].

[242]Cm has an increased share of the decay heat compared to the PWR due to the presence of TRU in the U/TRU-Zr10% fuel results in increased production of [242]Am, which decays into [242]Cm.
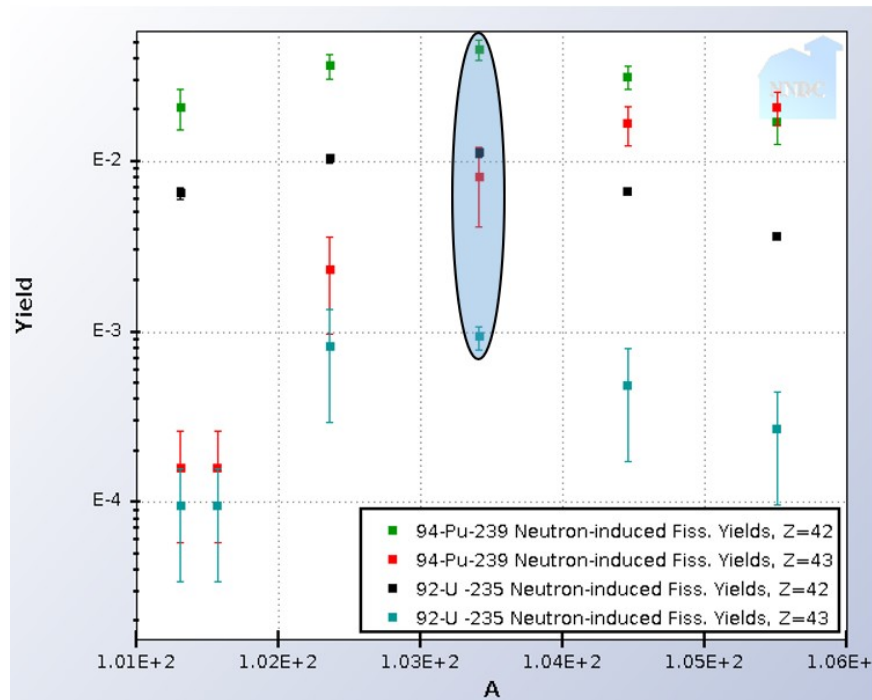
Figure 13. Comparison of ^{235}U and ^{239}Pu direct fission yields for [104]Mo (Z=42) and [104]Tc (Z=43). Data and image taken from the online NNDC SIGMA plotter [14].

Figure 14 shows the relative contributions of actinides and non-actinides to the total decay heat for both the representative PWR and the ABTR. Notably, the point at which fission products no longer contribute the majority of the decay heat is substantially earlier following shutdown in the ABTR relative to the PWR. Expressed in years, this point is approximately 60 years following shutdown for the PWR and 3 years for the ABTR. Although this time scale is not particularly relevant for accident progression analysis, it demonstrates the transmutation of TRU fuel into fission products with the earlier decrease in relative contribution to the decay heat from the actinides. Again, this result might include a small bias from the use of the LFPs at BOEC such that the initial concentration of fission products, in particular long-lived fission products, was neglected.
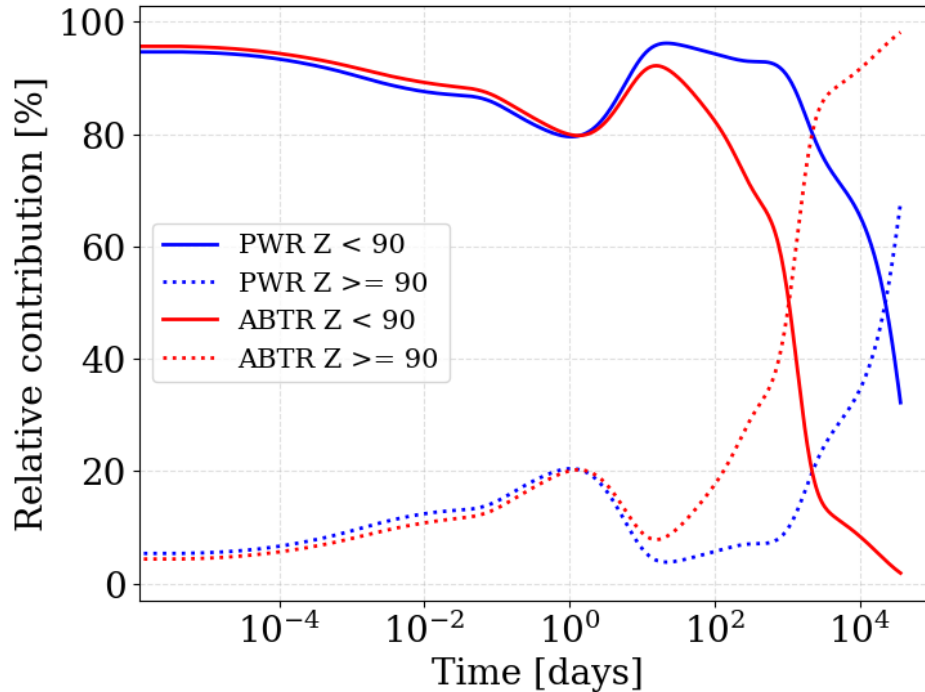
Figure 14. Comparison of ABTR and reference PWR decay heat contributions by actinides and non-actinides following shutdown.

5.2 POWER PROFILES

To allow for an analysis of the power profiles with TRITON, the nominal KENO-VI model was modified to model each assembly independently with a unique material ID, with axial discretization further dividing each assembly into 10 equal volume segments. This resulted in a TRITON–KENO-VI model with 600 depletion zones. Preliminary results noted in Section 4.2 investigating fission and flux rates were performed to inform and ensure that this axial discretization was suitable in capturing spatial effects of the reactor. As expected for a fast reactor, the long neutron mean free path causes fewer variable power profiles compared to that of thermal systems. The following sections detail the observed power profiles, as well as the condensation of 600 zones into an axially integrated radial power profile, a core-average axial profile, and assembly group-wise radial powers for MELCOR.

5.2.1 Radial Power

The ABTR contains 60 fuel assemblies that are modeled individually in the TRITON–KENO-VI model. Additionally, each assembly was subdivided into 10 axial zones. Therefore, TRITON provides an assembly-segmented and axially segmented data set of inventories and powers. To analyze the radial power profile, the power in each assembly was axially integrated using mass weighting based on the masses in the individual segments. Although masses are nearly uniform, there are slight deviations based on the burnup and rounding from axially splitting the volume fractions. The normalized EOEC radial power profile of ABTR is presented in Figure 15. Although TRITON does not propagate statistical uncertainties from the Monte Carlo calculation to the mixture power estimates, Section 5.2.3 describes an external estimate of statistical error of the radial power profile that determines these estimates to be well converged. The convergence is also evident in the symmetry of Figure 15.

Typical severe accident models in MELCOR model the power axially and radially (in rings). However,
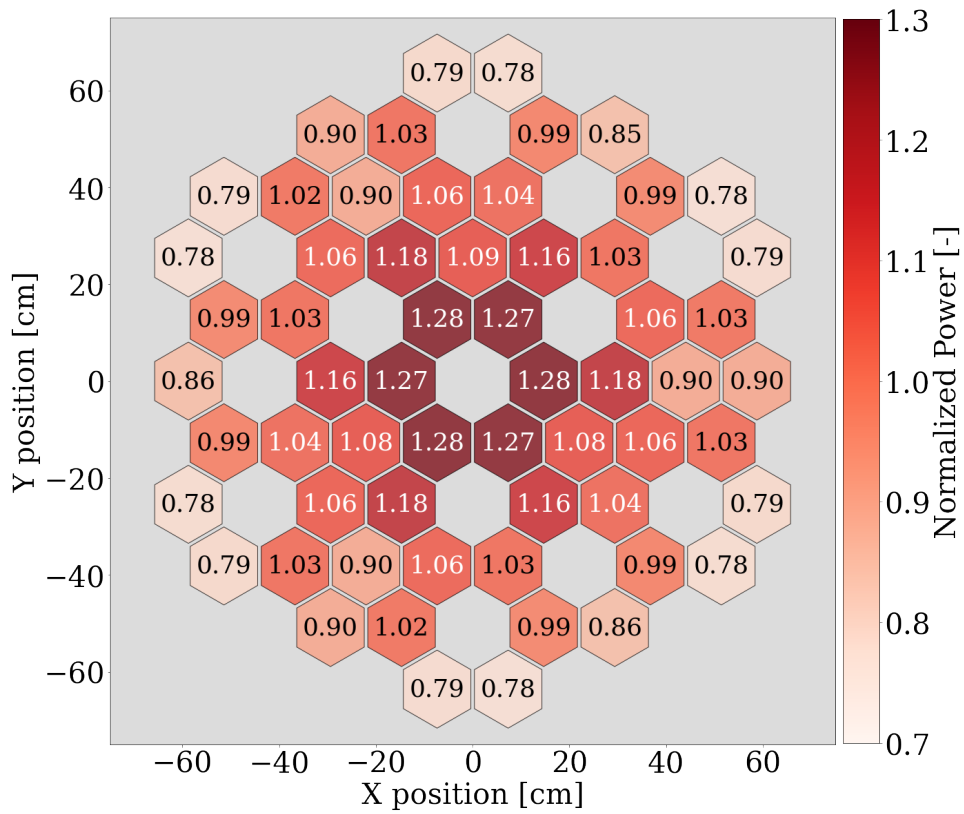
Figure 15. Axially integrated normalized EOEC radial power distribution.

providing a radial profile for the ABTR, accounting for control and test assemblies, would lead to nonconservative power values for each ring. Instead, assemblies were grouped based on similar power levels, which resulted in less variability within the groups. Five groups were determined, based on the normalized, axially integrated powers in Figure 15.

The bins used to group assemblies by normalized power are detailed in Table 10, as is the average normalized power of the assemblies that fall within the group. These group averages were provided along with the axial power profile to the MELCOR team. Groups are structured to move generally toward the center of the core with increasing group number (e.g., group 1 on the periphery, group 5 at the center, see Figure 16).

Table 10. Grouping of normalized axially integrated power

Radial grouping	Lower limit	Upper limit	Average
1 (Periphery)	0.7	0.9	0.799
2	0.9	1.0	0.946
3	1.0	1.1	1.048
4	1.1	1.2	1.169
5 (Center)	1.2	1.3	1.274
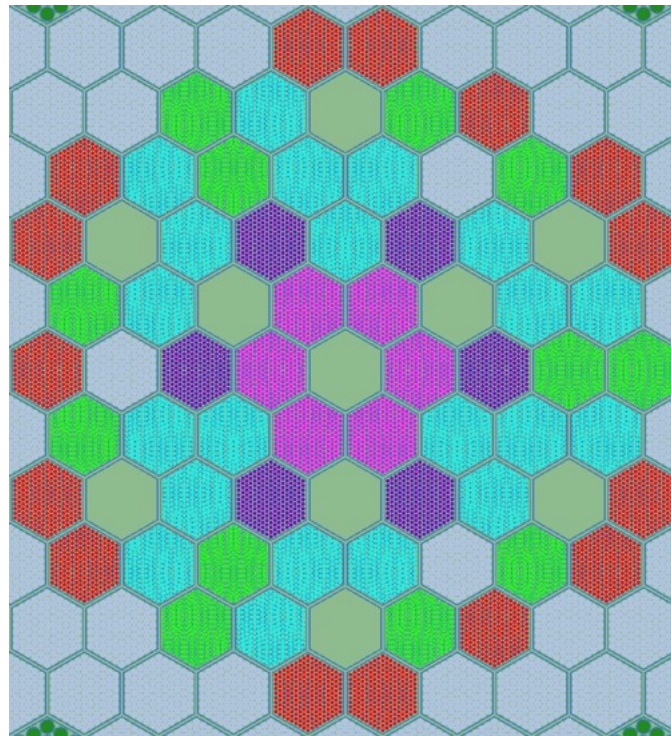
Figure 16. Groups of fuel assemblies with similar power. Group 1 (red), Group 2 (green), Group 3 (blue), Group 4 (purple), Group 5 (pink).

5.2.2   Axial Power

Normalized axial power profiles were determined for each assembly, assembly group (see Figure 16), and the core. The variation of axial profiles across the individual fuel assemblies and assembly groups was minimal as shown in Figure 17. The difference between the axial power profile of the assembly group and the core is

below 1% in in all zones, other than the upper most axial zones, in which slightly larger differences of up to 3% occur due to increased leakage in the absence of an upper reflector and the presence of absorber assemblies. A similar variability was not found in the lower axial zone because of the reflector that is consistently below all assemblies. The definitions of the axial zone boundaries and the core power profile is shown in Table 11.
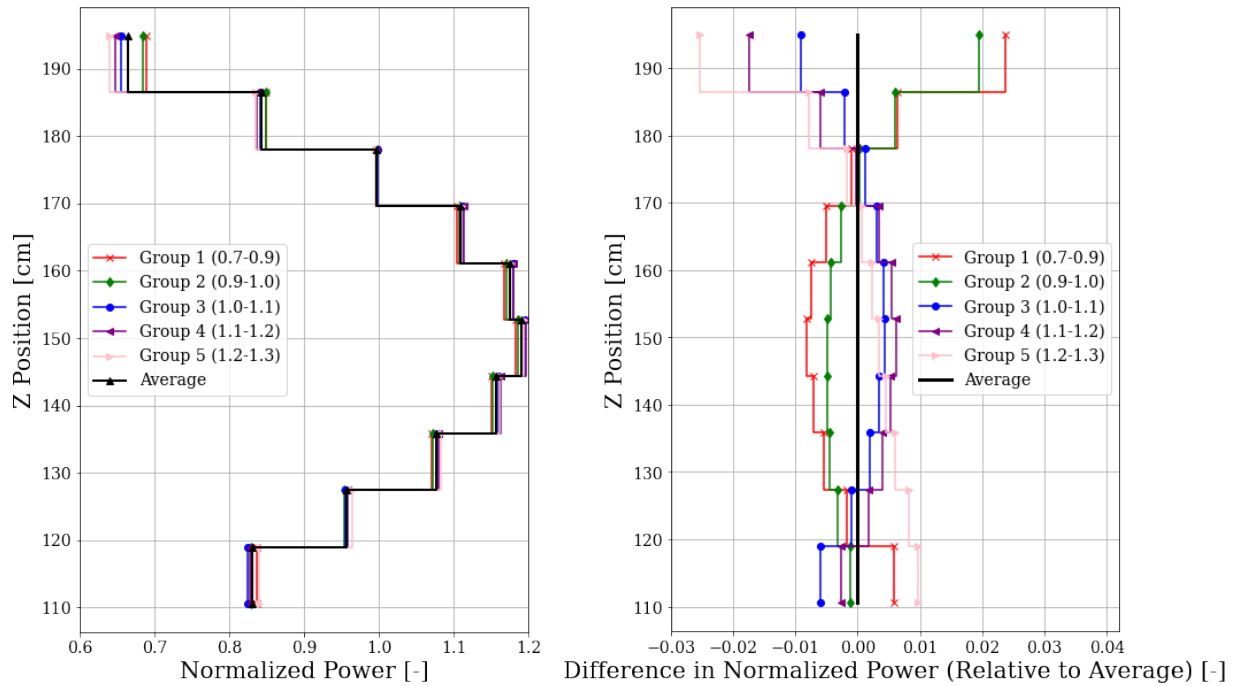
Figure 17. Axial power profiles of assembly groups compared with the core axial profile (denoted "Average" in the figure).

Table 11. Core axial power profile

Axial zone	Lower bound (cm)	Upper bound (cm)	Power (-)
10 (Top)	186.50272	194.94380	0.666
9	178.06164	186.50272	0.844
8	169.62056	178.06164	0.997
7	161.17948	169.62056	1.109
6	152.73840	161.17948	1.174
5	144.29732	152.73840	1.190
4	135.85624	144.29732	1.156
3	127.41516	135.85624	1.076
2	118.97408	127.41516	0.957
1 (Bottom)	110.53300	118.97408	0.831

5.2.3 Effect of Single-Assembly Sodium Voiding

Three accidents were to be analyzed with MELCOR based on this work: an unprotected transient over-power, an unprotected loss of flow, and a single blocked fuel assembly [16]. To avoid making assumptions about the effect of the single blocked assembly on the power profile and the void coefficient, a TRITON model with

one voided fuel assembly was developed to demonstrate the perturbation of the power distribution that results from a blocked assembly. This is particularly relevant given the spatial dependence of the void coefficient [19]. In the highest power assembly, located in the inner ring, the sodium coolant within the duct was voided from the bottom of the active core to the top of the upper core structure. In a second model, the additional bypass coolant between the ducts was voided. The different models of sodium voiding are shown in Figure 18.

| (a) Unvoided. | (b) Duct voiding | (c) Duct and peripheral voiding |
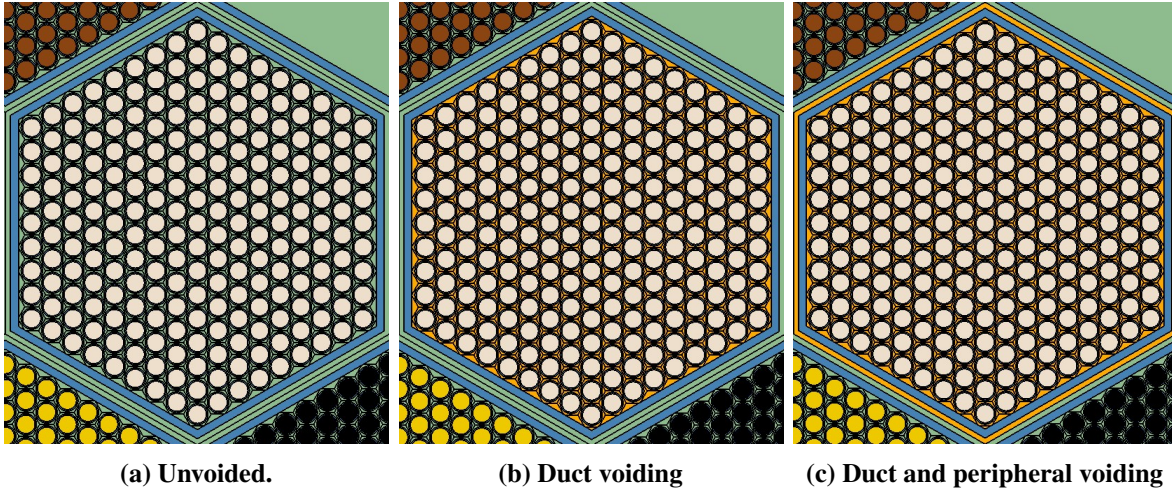
**Figure 18. Sodium coolant voiding (orange) modeling approaches.**

Table 12 notes the variation in k_{eff} due to these different voiding approaches. Voiding a single assembly has a negligible effect on the eigenvalue, with Δk_{eff} near statistical insignificance. Note that the voided assembly for this analysis is a high-powered central assembly. The selection of this assembly was intended to inform handling of the MELCOR analysis and is not expected to be representative of all other assemblies. Prior research has demonstrated that SFRs typically have an increased void worth at the center of the core, decreasing toward the periphery [19]. A very small positive effect caused by local spectrum hardening was observed—see Section 5.2.4 for further details.

Table 12. EOEC single assembly coolant void worth

Case	k_{eff}	Difference (pcm)
Nominal	1.01617 ± 0.00003	(ref)
Duct voiding	1.01632 ± 0.00004	15 ± 5
Duct and peripheral voiding	1.01638 ± 0.00004	21 ± 5
Nominal (average of 10)	1.01614 ± 0.00002	(ref)
Duct voiding (average of 10)	1.01634 ± 0.00002	20 ± 2

Figure 19 shows the effect of the single assembly voiding on the radial power profile. The upper Figure 19a shows only a small deviation in the innermost assembly ring and especially the voided assembly. Figure 19b shows the relative differences in power. All but two assemblies have a variation in power of less than 0.1 MW/MTIHM, while as a percent on the nominal power, approximately two-thirds have variations of less than 0.1%. The specific voided assembly is evident and shows a difference of 0.7% in power. Ultimately, this difference was deemed small enough that an update of the modeling to account for this effect was not pursued.
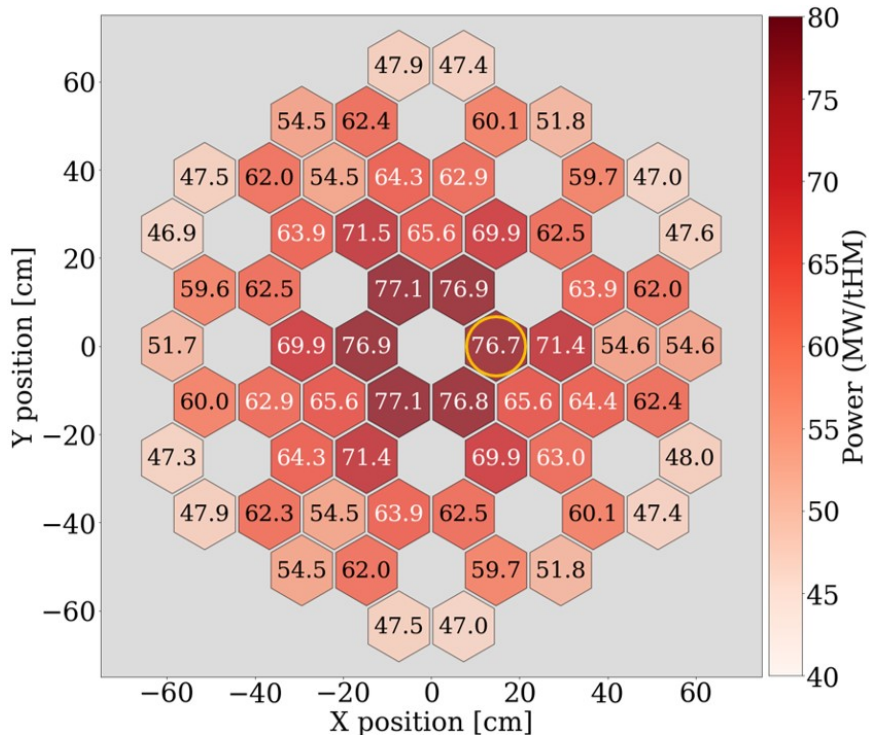
(a) Power distribution with a voided (circled) assembly
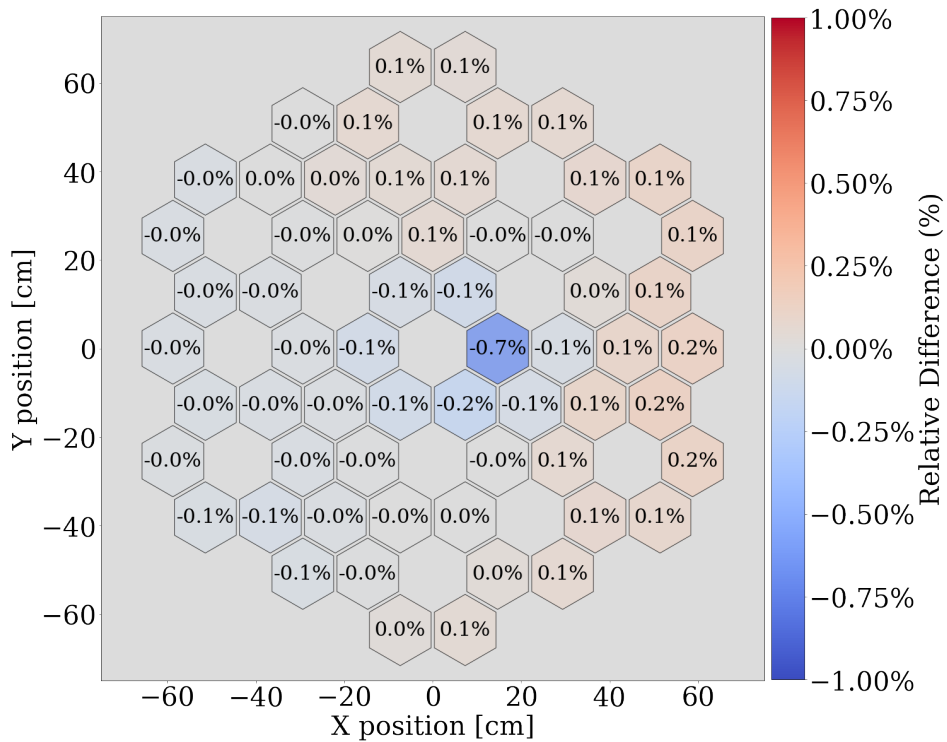
(b) Relative power difference between voided and nominal

Figure 19. Effect of single assembly sodium voiding on axially integrated radial power distribution.

5.2.4 External Calculation of the Statistical Uncertainty

Figure 19b shows 39 assemblies with less than a 0.1% power variation between the nominal and voided condition, whereas another 17 assemblies saw less than a 0.2% variation. In all, 56 of the 60 assemblies had less than a 0.2% change in power with sodium voiding. To assess whether these small differences were caused only by statistical uncertainties of the Monte Carlo calculation, external estimates of the statistical uncertainty of the power profile for the nominal and the assembly-voided cases was performed by averaging the results of 10 Monte Carlo calculations with different random seeds. This analysis found that the average of these 10 calculations results in a maximum standard deviation of 0.1% for the assembly powers under voided and nominal conditions. Figure 20 shows the absolute standard deviation of the nominal radial power profile and the relative difference in radial power between the assembly-voided and the nominal calculation in terms of statistical standard deviations.

These results show that (1) any small deviation in the nominal power profile (Figure 15) from symmetry is likely caused by statistical fluctuations and (2) that the effect on power through the assembly voiding is the result of statistical noise for all but the central fuel assemblies. The voided assembly has a power difference of 17 standard deviations compared with the nominal power and is therefore clearly statistically significant. Note that the values in Figure 20b are all positive, reflecting the magnitude of the effect but not the direction. The voiding performed here always results in a negative power shift on the voided assembly.
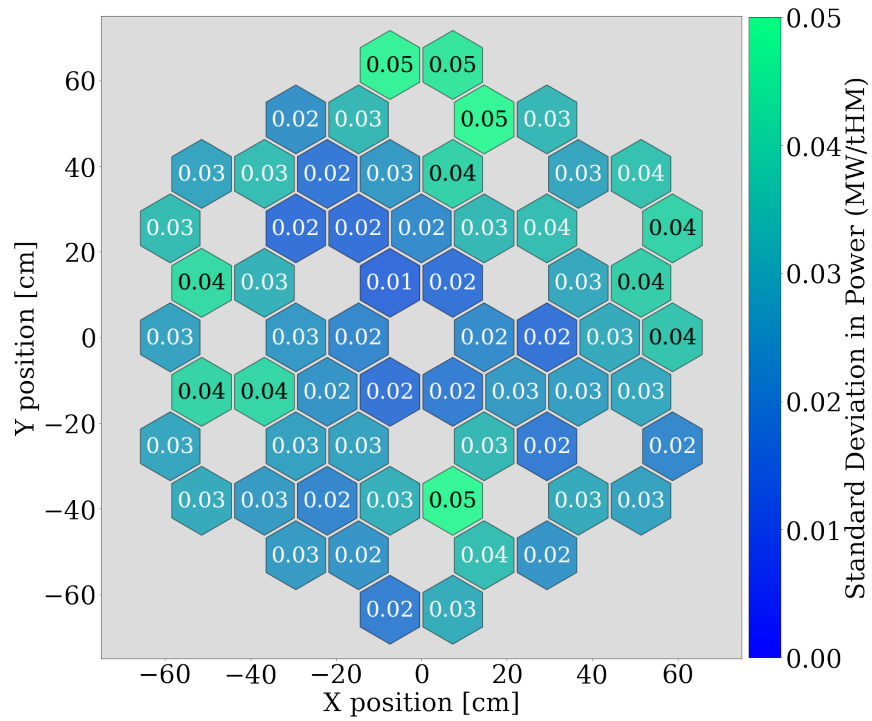
(a) Standard deviation in the power distribution
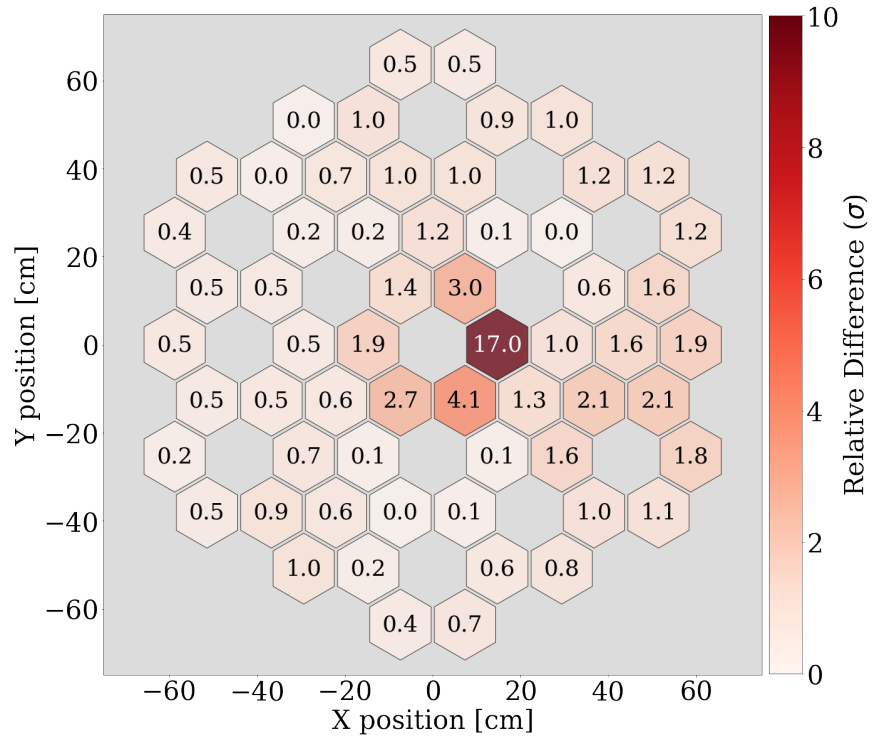
(b) Difference in power divided by estimated standard deviation

Figure 20. Random number seed averaging of nominal and voided power distributions.

5.3 XENON REACTIVITY AND EFFECTIVE DELAYED NEUTRON FRACTION AT EOEC

This section describes the calculations to confirm the xenon worth behavior after shutdown can be ignored in MELCOR point kinetics calculations for the ABTR. Three CSAS[2] calculations were performed: (1) a nominal CSAS calculation, (2) an otherwise identical CSAS calculation with all ^{135}Xe fission products removed, and (3) an otherwise identical CSAS calculation with only the PFNS to re-calculate β_{eff} at EOEC. Results of these calculations are presented in Table 13.

As expected, the ^{135}Xe worth at EOEC is within statistical noise of the Monte Carlo calculation. β_{eff} was calculated again with the Bretscher prompt k_{eff} ratio. The obtained value of 344 ± 5 pcm is within the statistical uncertainty of the value at BOEC of 331 ± 5.

Table 13. EOEC xenon worth and prompt k_{eff}

Case	k_{eff}	Difference (pcm)
Nominal	1.01617 ± 0.00003	(ref)
No Xe-135	1.01609 ± 0.00003	−9 ± 5
PFNS	1.01273 ± 0.00004	−344 ± 5

---

[2]A new capability was used to streamline this analysis where the EOEC inventory generated by TRITON was reformatted into standard composition blocks by the new OBIWAN utility.

6. ORIGEN REACTOR LIBRARY GENERATION

The objective of developing an ORIGEN reactor library for the ABTR is to enable rapid depletion calculations for the generation of nuclide inventory using ORIGAMI. Moreover, using the latest enhancements to ORIGAMI for non-LWRs, the equilibrium core search for the ABTR can also be conducted. Therefore, the library was produced for both startup and equilibrium cores. The startup core has the same dimensions and number of assemblies as the equilibrium core. However, the TRU enrichment in the startup fuel assembly is slightly lower than in the equilibrium core. The TRU enrichment in the startup core is 16.5%, 20.7%, and 18.7% for the inner, outer, and test assemblies, respectively. Additionally, the test assembly has a TRU vector obtained from LWR spent fuel TRU, whereas the TRU vector from weapons-grade plutonium was used for both the inner and outer assemblies [6].
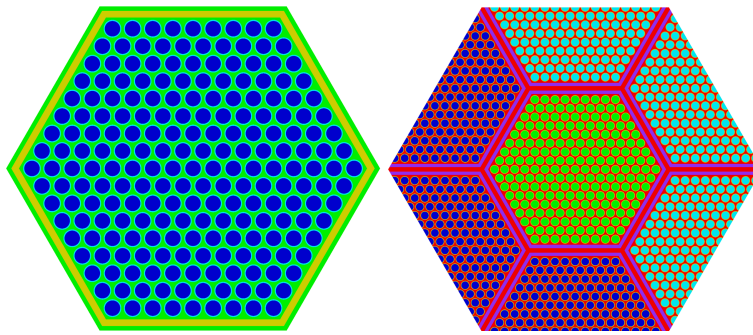
Figure 21. Two-dimensional inner and outer (left) and test (right) fuel assembly models.

Several sensitivity calculations were conducted to generate reliable ORIGEN libraries and to assess the parameters affecting the one-group cross section data stored on the library. A 2D lattice model with reflective boundary conditions (Figure 21) was used to perform the rapid evaluation. The 2D lattice model can be used to reliably generate ORIGEN libraries for LWRs. In this study, the inner and outer assemblies were modeled as a single fuel lattice. However, the test assembly was modeled as a supercell model in which it is surrounded by an equal number of inner and outer fuel assemblies as it is located in the core. Using this modeling approach, the one-group removal and fission cross sections of major heavy metals from several fuel assemblies with different TRU enrichments are compared in Figure 22. The removal cross section of fertile nuclides is not affected by the TRU enrichment. However, the cross section of the fissile nuclides slightly decreases when the TRU enrichment increases.

Using a single fuel lattice model containing 20.7% weapons-grade plutonium, the effect of temperature changes in the fuel, sodium coolant, and HT-9 structural material on the one-group cross section was also assessed. In this evaluation, the temperature was limited to the inlet, average, and outlet temperatures. Moreover, the density of the sodium coolant changed according to its temperature. As illustrated in Figures 23, 24, and 25, the temperature of each component has a negligible effect on the one-group cross section, with the three temperatures' effects visually indistinguishable. The one-group cross section is also provided as a function of burnup, and the one-group cross section varies little with burnup, implying that the neutron spectrum changes little with burnup.

Lastly, for verification, the one-group cross section generated by the 2D assembly lattice model was compared with one directly produced by the 3D core model as depicted in Figure 26. The one-group cross section for the outer fuel assembly produced by the 2D lattice model has a significant discrepancy. The spectrum in the outer fuel is less hardened since it is located near the HT-9 radial reflector, as shown in

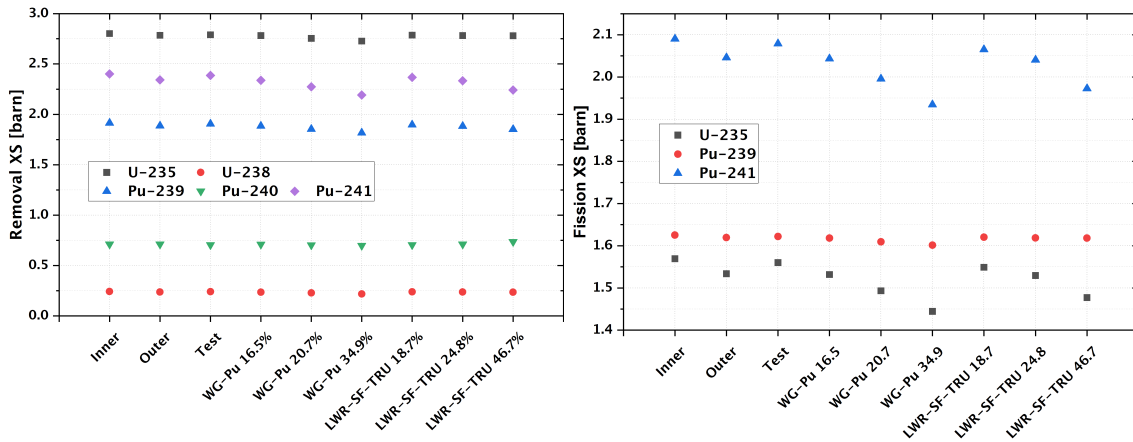**Figure 22. One-group cross sections as a function of TRU enrichment in a 2D lattice model.**

Figure 23. One-group cross sections as functions of burnup and fuel temperatures in a 2D lattice model. Temperature effects are visually indistinguishable.

Figure 24. One-group cross sections as functions of burnup and coolant temperatures in a 2D lattice model. Temperature effects are visually indistinguishable.
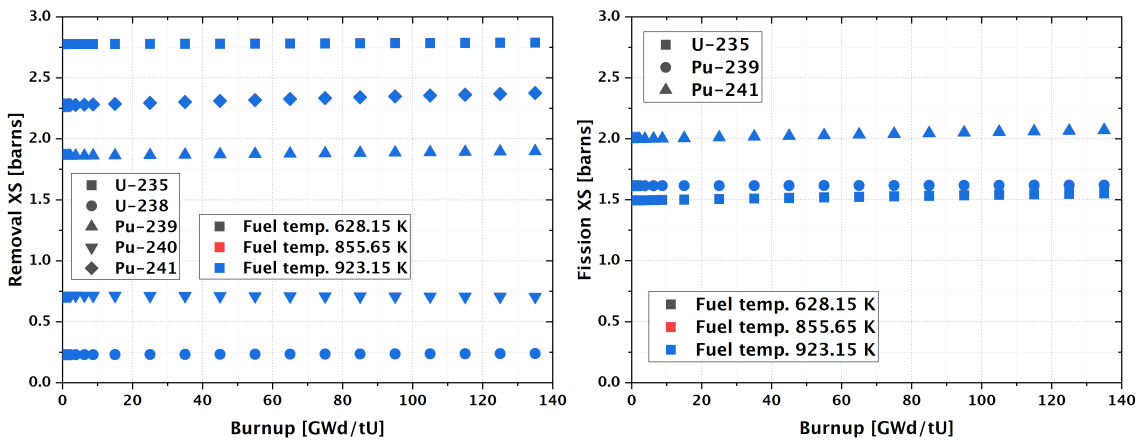
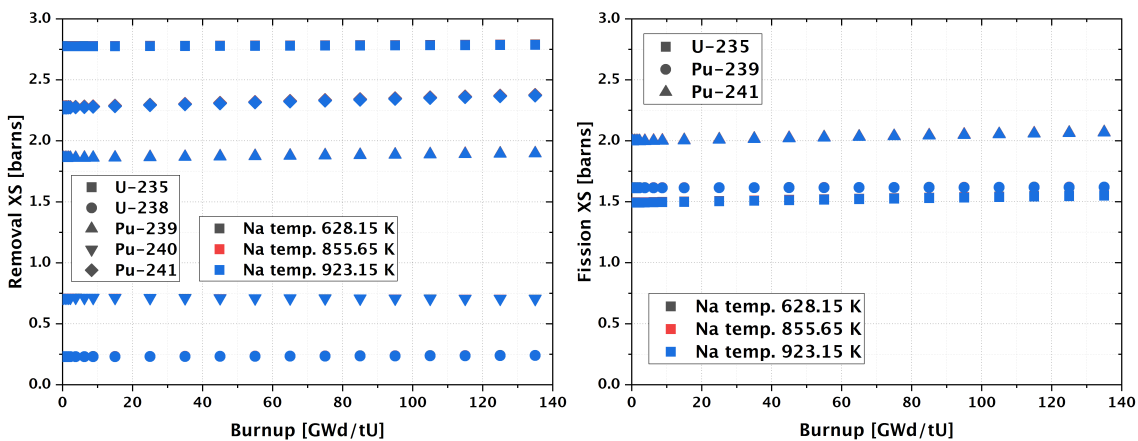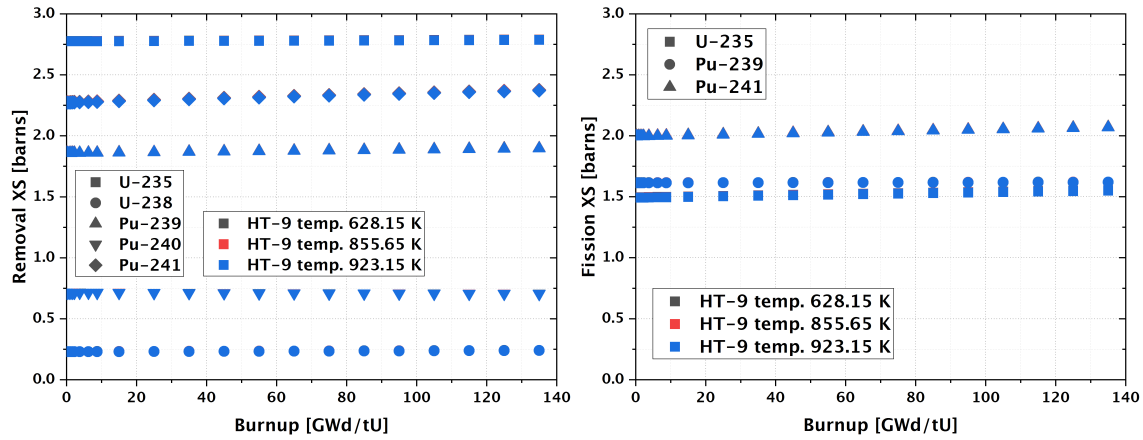**Figure 25. One-group cross sections as functions of burnup and HT-9 temperatures in a 2D lattice model.** Temperature effects are visually indistinguishable.

Figure 27, but it cannot be captured correctly by using a 2D lattice model. As a trade-off between accuracy and computing time, the axial slice core model can be used to generate the one-group cross section. In fact, the slice core model has been extensively adopted in generating the cross section for other non-LWRs [17, 1]. The axial slice core model is a 2D core model, a slice through the center of the core, with a vacuum boundary condition in the radial direction and a reflective boundary condition in the axial direction. Using this model, the maximum absolute relative error of the major nuclides' one-group cross section is about 1.5%.

Based on these findings, a set of ORIGEN libraries was generated for the ABTR-250, parameterized for assembly position in the core (inner, test, and outer) and the TRU enrichment. These libraries can be used to rapidly predict the ABTR-250 inventory with ORIGAMI under varying conditions without having to run computationally intense, detailed full-core depletion calculations.
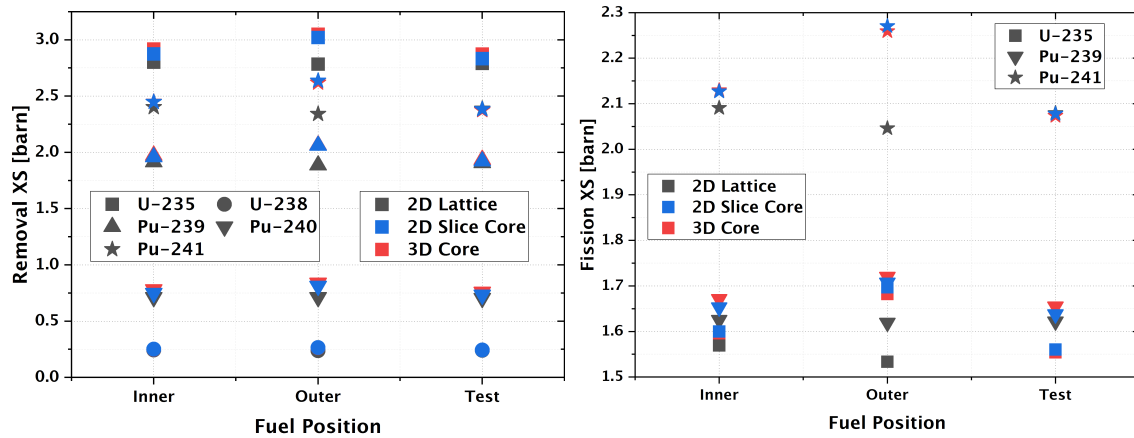
Figure 26. One-group cross sections by 2D lattice, 2D axial slice core, and 3D core models.
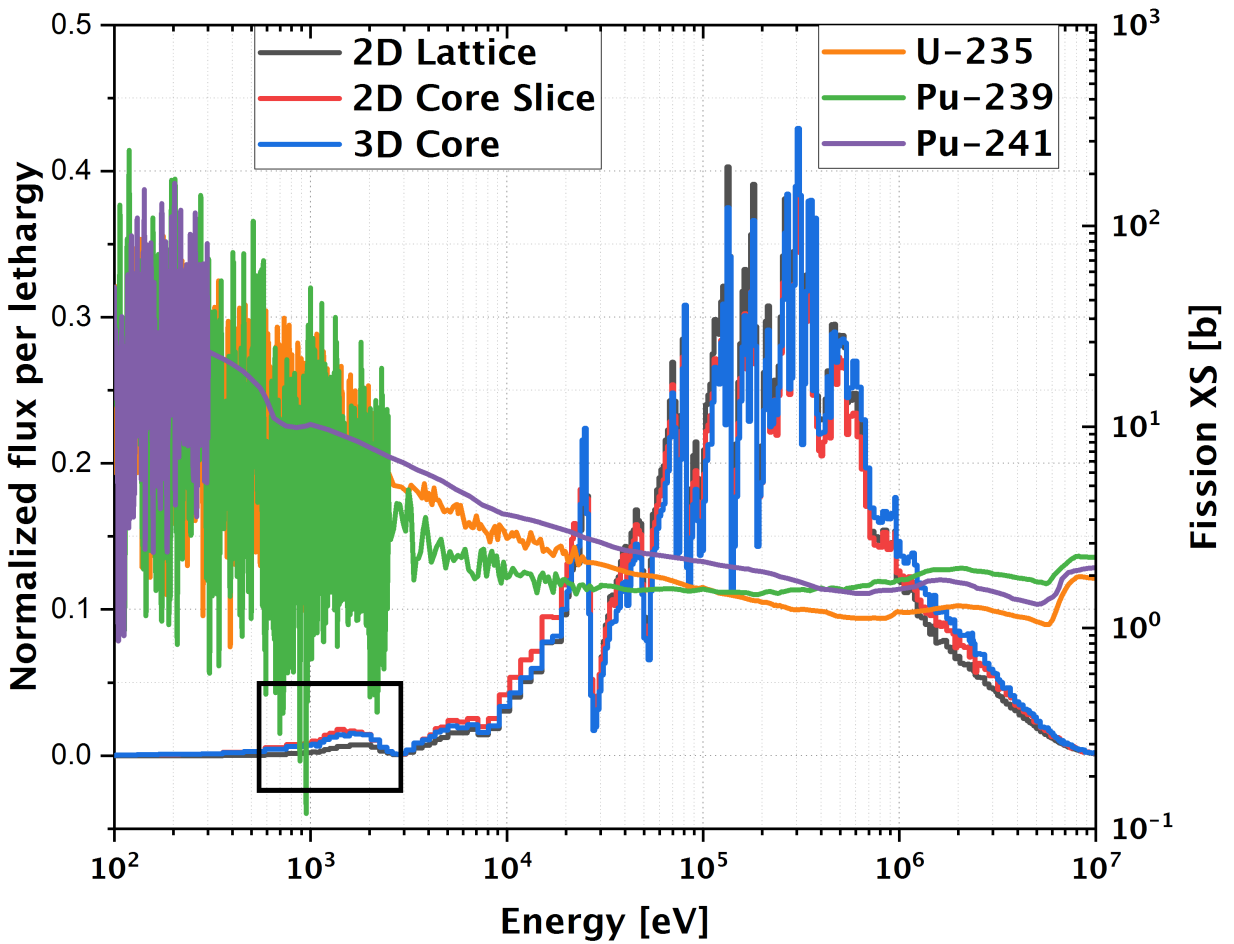
Figure 27. Comparison of outer fuel assembly neutron flux for different models. The left y-axis defines the normalized flux per lethargy, and the right y-axis is for the microscopic fission cross section of fissile uranium and plutonium.

7. CONCLUSIONS

With rising interest in non-LWR reactor designs from commercial entities, the NRC must ensure that upon receiving a licensing application, the available tools and data are capable of accurately and efficiently analyzing such systems. As part of an NRC-sponsored project, the SNL MELCOR team and the ORNL SCALE team are collaborating to assess the modeling and simulation capabilities for accident progression, source term, and consequence analysis for non-LWR technologies. SCALE is being used to provide MELCOR with nuclide inventories, reactivity feedback coefficients, power distributions, and decay heat based on results obtained with the SCALE/CSAS and SCALE/TRITON sequences and the depletion solver ORIGEN. With this information, MELCOR can be used to perform severe accident progression and source term analyses. This report summarizes the ORNL analysis using SCALE for a benchmark ABTR reactor design which represents the SFR class of reactors. The report is intended as a demonstration of SCALE capabilities and does not reflect a safety analysis of the ABTR.

A SCALE model of the BOEC ABTR was developed based on publicly available specifications. SCALE results of the eigenvalue and effective delayed neutron fraction were verified by comparison with published results from other codes. Excellent agreement was demonstrated for both output quantities. Based on the verified model, the subsequent analysis was divided into three parts: (1) BOEC CSAS–KENO full-core neutronics analysis, (2) generation of EOEC fuel inventory and power profile analysis using TRITON–KENO full core depletion, and (3) ORIGEN reactor library generation.

The CSAS–KENO BOEC calculations resulted in flux distributions, reactivity coefficients, and control assembly worth verification. Reactivity coefficients were determined for geometrical and material density changes (corresponding to temperature changes in the affected material), fuel temperature change, sodium void worth, and control rod worth. All reactivity coefficients were found to be negative. Whereas most reactivity coefficients were calculated via direct perturbation of the model, the fuel Doppler reactivity coefficient was determined from a logarithmic fitting of the reactivity over the temperature. Verification of these reactivity effects was limited to the control rod worths, which showed good agreement with published results, with a minor trend of increasing deviation between results with increased spectral hardening. The calculations performed in this report are described in detail, and a corresponding public repository provides all inputs related to this analysis to allow for future replication.

Following the BOEC analysis, a TRITON–KENO full-core depletion calculation was performed for a single cycle to produce detailed EOEC nuclide inventories that were used to calculate decay heat and power distributions at EOEC. The decay heat in % operating power was found similar between the ABTR and a PWR, with just above 5% operating power right after shutdown. When comparing the individual contributors to the decay heat, differences in contributions from individual nuclides were observed due to fission of different fissile nuclides (U vs. Pu) at different energies (thermal vs. fast). The ABTR results were further slightly biased by using lumped fission products in the BOEC fuel so that the EOEC inventory disregards the amount of long-lived fission products existing at the beginning of the cycle. Detailed axial and radial power profiles were determined with external assessments of the statistical uncertainty via multiple runs with different random number seeds. In support of the MELCOR analysis of a fuel assembly blockage accident scenario, the effect of a single fuel assembly voiding on reactivity and on the power profile was determined. The voiding of a single fuel assembly in the inner core resulted in a 0.7% power reduction for the voided assembly, and nearly all other power variations were statistical insignificant. In terms of reactivity, a very small positive reactivity effect (~20 pcm) was observed as a result of spectrum hardening from the loss of sodium in this assembly.

Results obtained by SCALE were postprocessed to provide the MELCOR team with the EOEC inventory, decay heat, axial and radial power profiles, and temperature feedback coefficients. All inputs, outputs, and files for data processing are available from a public Gitlab repository accompanying this report.[3]

A final objective, though not directly in support of accident progression for MELCOR analysis at this time, was the generation of an ORIGEN reactor library for the ABTR. Sensitivity studies were performed to identify an adequate surrogate model and to identify relevant parameters for which libraries should be generated. Variations in one-group fission and removal cross sections were determined for a range of relevant parameters, such as TRU enrichment, burnup, and material temperatures. An axially reflected slice model through the center of the ABTR core was found to be adequate for the library generation, providing a compromise between accuracy and computing time. The one-group cross sections showed minor dependence on burnup and examined material temperatures, requiring the library generation to only consider parameterization for the fuel assembly position in the core and for the TRU enrichment. These ORIGEN reactor libraries will provide the basis for future rapid inventory calculations with SCALE's ORIGAMI code.

---

[3]https://code.ornl.gov/scale/analysis/non-lwr-models-vol3.

REFERENCES

[1] F. Bostelmann, C. Celik, R. F. Kile, and W. A. Wieselquist. SCALE Analysis of a Fluoride Salt-Cooled High-Temperature Reactor in Support of Severe Accident Analysis. Technical Report ORNL/TM-2021/2273, Oak Ridge National Laboratory, Oak Ridge, TN, 2022. doi:10.2172/1854475.

[2] F. Bostelmann, G. Ilas, C. Celik, A. M. Holcomb, and W. A. Wieselquist. Nuclear Data Assessment for Advanced Reactors. Technical Report NUREG/CR-7289, ORNL/TM-2021/2002, Oak Ridge National Laboratory, Oak Ridge, TN, 2021. doi:10.2172/1840202.

[3] F. Bostelmann, G. Ilas, and W. A. Wieselquist. Nuclear Data Sensitivity Study for the EBR-II Fast Reactor Benchmark Using SCALE with ENDF/B-VII.1 and ENDF/B-VIII.0. *Annals of Nuclear Energy*, 132:161–171, 2019. doi:10.1016/j.anucene.2019.04.034.

[4] F. Bostelmann, B. T. Rearden, W. Zwermann, and A. Pautz. SCALE/AMPX Multigroup Libraries for Sodium-Cooled Fast Reactor Systems. *Annals of Nuclear Energy*, 140:107102, 2020. doi:10.1016/j.anucene.2019.107102.

[5] M. M. Bretscher. Evaluation of reactor kinetics parameters without the need for perturbation codes. In *1997 International Meeting on Reduced Enrichment for Research and Test Reactors*, 1997. URL: https://www.osti.gov/etdeweb/servlets/purl/20521144.

[6] Y. I. Chang, P. J. Finck, and C. Grandy. Advanced Burner Test Reactor Preconceptual Design Report. Technical Report ANL-ABR-1 (ANL-AFCI 173), Argonne National Laboratory, Argonne, IL, 2006. doi:10.2172/946035.

[7] J. K. Fink and L. Leibowitz. Thermodynamic and Transport Properties of Sodium Liquid and Vapor. Technical Report ANL/RE-95/2, Argonne National Laboratory, 1995. URL: https://inis.iaea.org/search/search.aspx?orig_q=RN:27004412.

[8] L.L. Humphries, B.A. Beeny, F. Gelbard, D.L. Louie, and J. Phillips. MELCOR Computer Code Manuals - Vol. 1: Primer and Users' Guide. Technical Report SAND2017-0455 O, Sandia National Laboratories, Albuquerque, NM, 2017.

[9] Dawn E. Janney. Metallic Fuels Handbook, Part 1: Alloys Based on U-Zr, Pu-Zr, U-Pu, or U-Pu-Zr, Including Those with Minor Actinides (Np, Am, Cm), Rare-earth Elements (La, Ce, Pr, Nd, Gd), and Y. Technical Report INL/EXT-15-36520, Idaho National Laboratory, Idaho Falls, ID, 2017. doi:10.2172/1504934.

[10] K. S. Kim, M. L. Williams, A. M. Holcomb, D. Wiarda, B. K. Jeon, and W. S. Yang. The SCALE/AMPX multigroup cross section processing for fast reactor analysis. *Annals of Nuclear Energy*, 132:161–171, 2019. doi:10.1016/j.anucene.2019.04.034.

[11] T. K. Kim. Benchmark Specification of Advanced Burner Test Reactor. Technical Report ANL-NSE-20/65, Argonne National Laboratory, Argonne, IL, 2020. doi:10.2172/1761066.

[12] A. Lo, F. Bostelmann, D. Hartanto, B. Betzler, and W. A. Wieselquist. Application of SCALE to Molten Salt Fueled Reactor Physics in Support of Severe Accident Analyses. Technical Report ORNL/TM-2022/1844, Oak Ridge National Laboratory, Oak Ridge, TN, 2022. doi:10.2172/1897864.

[13] C. M. Mueller, Ching-Sheng Lin, and Javier Ortensi. NRC Multiphysics Analysis Capability Deployment FY2021 – Part 2. Technical Report INL/EXT-21-62522, Idaho National Laboratory, Idaho Falls, ID, 2021. doi:10.2172/1812179.

[14] NNDC. Evaluated Nuclear Data File (ENDF) Retrieval And Plotting. https://www.nndc.bnl.gov/sigma/, 2022. Accessed: August 24, 2022.

[15] NRC. Pre-Application Activities for Advanced Reactors. https://www.nrc.gov/reactors/new-reactors/advanced/licensing-activities/pre-application-activities.html, 2022. Accessed: August 24, 2022.

[16] NRC. SCALE/MELCOR Non-Light-Water Reactor (Non-LWR) Source Term Demonstration Project - Sodium-Cooled Fast Reactor. https://adamswebsearch2.nrc.gov/webSearch2/main.jsp?AccessionNumber=ML22262A252, 2022. Accessed: October 3, 2022.

[17] Steven E. Skutnik and William A. Wieselquist. Assessment of ORIGEN Reactor Library Development for Pebble-Bed Reactors Based on the PBMR-400 Benchmark. Technical Report ORNL/TM-2020/1886, Oak Ridge National Laboratory, Oak Ridge, TN, 2021. doi:10.2172/1807271.

[18] N. Stauff. Status of the NEAMS and ARC Neutronic Fast Reactor Tools Integration to the NEAMS Workbench. Technical Report ANL/NEAMS-20/2, Argonne National Laboratory, Argonne, IL, 2020. URL: https://publications.anl.gov/anlpubs/2020/10/162841.pdf.

[19] N. Stauff, T. Fei, and M. Smith. ARDP Natrium Neutronic Methodology: Argonne Neutronic Assessment of ABR-1000. Technical Report ANL/NSE-22/31, Argonne National Laboratory, 2022. doi:10.2172/1875808.

[20] James W. Sterbentz, James E. Werner, Andrew J. Hummel, John C. Kennedy, Robert C. O'Brien, Axel M. Dion, Richard N. Wright, and Krishnan P. Ananth. Preliminary Assessment of Two Alternative Core Design Concepts for the Special Purpose Reactor. Technical Report INL/EXT-17-43212, Idaho National Laboratory, Idaho Falls, ID, 2018. URL: https://www.osti.gov/biblio/1413987.

[21] US NRC. NRC Non-Light Water Reactor (Non-LWR) Vision and Strategy, Volume 3: Computer Code Development Plans for Severe Accident Progression, Source Term, and Consequence Analysis. Technical Report ML20030A178, Rev. 1, US NRC, Rockville, MD, 2020. URL: https://www.nrc.gov/docs/ML2003/ML20030A178.pdf.

[22] D. C. Wade and E. K. Fujita. Trends Versus Reactor Size of Passive Reactivity Shutdown and Control Performance. *Nuclear Science and Engineering*, 103:182–195, 1989. doi:10.13182/NSE89-6.

[23] Kenneth Wagner, Bradley Beeny, , and David Luxat. MELCOR Accident Progression and Source Term Demonstration Calculations for a HTGR. Technical Report SAND2022-2750, Sandia National Laboratories, Albuquerque, NM, 2022. URL: https://www.osti.gov/biblio/1854083.

[24] Kenneth Wagner, Chris Faucett, Rod Schmidt, and David Luxat. MELCOR Accident Progression and Source Term Demonstration Calculations for a Heat Pipe Reactor. Technical Report SAND2022-2745, Sandia National Laboratories, Albuquerque, NM, 2022. URL: https://www.osti.gov/biblio/1854082.

[25] Kenneth Wagner, Troy Haskin, Bradley Beeny, Fred Gelbard, and David Luxat. MELCOR Accident Progression and Source Term Demonstration Calculations for a FHR. Technical Report SAND2022-2751, Sandia National Laboratories, Albuquerque, NM, 2022. URL: https://www.osti.gov/biblio/1854081.

[26] E. Walker, S. E. Skutnik, W. A. Wieselquist, Alex Shaw, and Friederike Bostelmann. SCALE Modeling of the Fast-Spectrum Heat Pipe Reactor. Technical Report ORNL/TM-2021/2021, Oak Ridge National Laboratory, Oak Ridge, TN, 2021. doi:10.2172/1871124.

[27] Alan E. Waltar, Donald R. Todd, and Pavel V. Tsvetkov. *Fast Spectrum Reactors*. Springer Science & Business Media, New York, USA, 2012.

[28] William A. Wieselquist and Benjamin Betzler. SCALE 6.2.4: Validation Overview. Technical Report ORNL/TM-2020/1500/v1, Oak Ridge National Laboratory, Oak Ridge, TN, 2022. doi:10.2172/1902803.

[29] William A Wieselquist, R. A. Lefebvre, and Matthew A. Jessee. SCALE Code System, Version 6.2.4. Technical Report ORNL/TM-2005/39, Oak Ridge National Laboratory, Oak Ridge, TN, 2020. URL: https://www.ornl.gov/file/scale-62-manual/display.

[30] Roald Wigeland. Review of Safety-Related SFR Experimental and Operational Experience in the United States. In *IAEA Workshop, Safety Aspects of Sodium Cooled Fast Reactors, IAEA Headquarters, Vienna, Austria, June 23–25*, 2010. URL: https://inis.iaea.org/search/search.aspx?orig_q=RN:49104076.

[31] W. S. Yang, T. K. Kim, S. J. Kim, and C. H. Lee. Preliminary Validation Studies of Existing Neutronics Analysis Tools for Advanced Burner Reactor Design Applications. Technical Report ANL-AFCI-186, Argonne National Laboratory, 2007. doi:10.2172/1508296.